



**HAL**  
open science

**Cell-intrinsic and -extrinsic functions of the ESCRT-III  
component Shrub in cytokinetic abscission  
of *Drosophila* Sensory Organ precursor**

Céline Bruelle, Mathieu Pinot, Emeline Daniel, Marion Daudé, Juliette  
Mathieu, Roland Le Borgne

► **To cite this version:**

Céline Bruelle, Mathieu Pinot, Emeline Daniel, Marion Daudé, Juliette Mathieu, et al.. Cell-intrinsic and -extrinsic functions of the ESCRT-III component Shrub in cytokinetic abscission of *Drosophila* Sensory Organ precursor. 2022. hal-03852439

**HAL Id: hal-03852439**

**<https://hal.science/hal-03852439>**

Preprint submitted on 15 Nov 2022

**HAL** is a multi-disciplinary open access archive for the deposit and dissemination of scientific research documents, whether they are published or not. The documents may come from teaching and research institutions in France or abroad, or from public or private research centers.

L'archive ouverte pluridisciplinaire **HAL**, est destinée au dépôt et à la diffusion de documents scientifiques de niveau recherche, publiés ou non, émanant des établissements d'enseignement et de recherche français ou étrangers, des laboratoires publics ou privés.

**Cell-intrinsic and -extrinsic functions of the ESCRT-III component Shrub in cytokinetic abscission of *Drosophila* Sensory Organ precursor**

Céline Bruelle<sup>1</sup>, Mathieu Pinot<sup>1</sup>, Emeline Daniel<sup>1</sup>, Marion Daudé<sup>1</sup>, Juliette Mathieu<sup>2</sup>  
and Roland Le Borgne<sup>1</sup>§

<sup>1</sup> Univ Rennes, CNRS, IGDR (Institut de Génétique et Développement de Rennes)  
UMR 6290, F- 35000 Rennes, France

<sup>2</sup> Center for Interdisciplinary Research in Biology (CIRB)  
UMR CNRS 7241 / INSERM U1050, Collège de France 11 place Marcelin Berthelot,  
75005 Paris, France

§ Corresponding author: R.L.B.

Orcid: <http://orcid.org/0000-0001-6892-278X>

e-mail: [roland.leborgne@univ-rennes1.fr](mailto:roland.leborgne@univ-rennes1.fr)

phone: +33 223 234 894

## Abstract

While the molecular mechanisms underlying the abscission of isolated cells are largely decrypted, those of fast-cycling, epithelial progenitors surrounded by epidermal cells (ECs) connected by junctions remain largely unexplored. Here, we investigated the remodeling of the permeability barrier ensured by septate junctions (SJs) during cytokinesis of *Drosophila* sensory organ precursor (SOP). We report that SOP cytokinesis involves the coordinated polarized assembly and remodeling of SJs in the dividing cell and its neighbors, which remained connected via membrane protrusions pointing toward the SOP midbody. SJs assembly and midbody basal displacement occur more rapidly in SOP than in ECs, leading to a faster disentanglement of the protrusions that precedes midbody release. As reported in isolated cells, the endosomal sorting complex required for transport-III component Shrub/CHMP4B is recruited at the midbody and cell-autonomously regulates abscission. In addition, we found that Shrub is recruited to membrane protrusions, is required for SJ integrity, and that alteration of SJ integrity leads to premature abscission. Our study uncovers cell- intrinsic and -extrinsic functions of Shrub in epithelial abscission to support the coordination of permeability barrier maintenance and abscission in SOPs.

## 1 **Introduction**

2 Cell junctions are essential for the chemical and mechanical functions of epithelia  
3 (Higashi et al., 2016). Adherens junctions (AJs) and Tight junctions (TJ) in  
4 vertebrates/ Septate Junctions (SJs) in invertebrate ensure the mechanical and  
5 permeability barriers respectively (Banerjee et al., 2006; Harris and Tepass, 2010;  
6 Shin et al., 2006; Tepass et al., 2001; Tsukita et al., 2001). *Drosophila* bicellular SJs  
7 (bSJs) are composed of a highly stable core complex containing more than 20  
8 proteins including–cytosolic proteins such as Coracle (Cora) and Disc-large (Dlg),  
9 Claudin-like proteins including Kune Kune, cell adhesion molecules such as Fasciclin  
10 III (Fas 3) transporters such as Na<sup>+</sup>/K<sup>+</sup> ATPase alpha (ATP $\alpha$ ) and beta (Nervana2  
11 (Nrv2)) subunits (Faivre-Sarrailh, 2020; Genova and Fehon, 2003; Izumi and Furuse,  
12 2014; Kaplan, 2002; Nelson et al., 2010; Snow et al., 1989; Ward et al., 1998). The  
13 localization of SJ components are interdependent of each other (Oshima and Fehon,  
14 2011).

15  
16 While cells need to establish and maintain proper permeability barrier, SJs remain  
17 highly plastic, especially during cell division, a fundamental process for the  
18 development and function of all organs. Abscission is the final step of cytokinesis  
19 that leads to the physical separation of the two daughter cells and has been  
20 proposed to help regulate cell fate acquisition (Chaigne et al., 2020; Ettinger et al.,  
21 2011). Cytokinesis is initiated at the onset of anaphase and begins with the formation  
22 of an actomyosin ring that constricts to ultimately form the midbody (Fededa and  
23 Gerlich, 2012; Glotzer, 2005; Green et al., 2012). The midbody present at the  
24 intercellular bridge connects the two daughter cells, and recruits effectors of  
25 abscission. In *Drosophila*, the centralspindlin protein complex recruits Alix to the  
26 midbody which in turn recruits the endosomal sorting complex required for transport-  
27 III (ESCRT III) component Shrub (the CHMP4B ortholog). Shrub/CHMP4B have the  
28 property to form homopolymers that are proposed to drive abscission (Eikenes et al.,  
29 2015; Guizetti et al., 2011; Lie-Jensen et al., 2019; Matias et al., 2015). In addition to  
30 being required for multivesicular body formation and abscission, CHMP4B exerts  
31 different functions including viral budding and, plasma and nuclear membrane  
32 resealing (Agromayor and Martin-Serrano, 2013; Lie-Jensen et al., 2019; Vietri et al.,  
33 2020). While there is a great deal of knowledge on the molecular mechanisms

34 underlying abscission of isolated cells, abscission in tightly packed polarized  
35 epithelial cells possessing junctional complexes remains largely under-explored.

36

37 Several studies have described that the formation of the new AJs is coordinated with  
38 the early steps of cytokinesis leading to the positioning of the midbody basal to the  
39 newly formed adhesive interface (Firmino et al., 2016; Founounou et al., 2013;  
40 Guillot and Lecuit, 2013; Herszterg et al., 2013; Higashi et al., 2016; Lau et al., 2015;  
41 Morais-de-Sá and Sunkel, 2013). It has also been showed that the neighbor cells  
42 maintain SJ contact with the dividing cell through SJ finger-like protrusions  
43 connected to the midbody in the *Drosophila* pupal notum and wing imaginal disc  
44 (Daniel et al., 2018; Wang et al., 2018). Novel SJ assembles below the AJs and  
45 spread basally concomitantly with the basal displacement of the midbody. Once the  
46 new SJ is formed, the midbody leaves the SJ about 1.5 hours after the onset of  
47 anaphase and abscission is taking place more than 5 hours post anaphase (Daniel  
48 et al., 2018; Wang et al., 2018). The sequence of events leading to abscission and  
49 junction remodeling is proposed to ensure the maintenance of the epithelial barrier  
50 functions in proliferative epithelia. This issue remains poorly characterized in  
51 epithelia composed of cells with distinct identities.

52

53 *Drosophila* notum consists of a single-layer epithelium with two types of cells,  
54 epidermal (EC) and sensory organs (SO) (Fig. 1A). Sensory organs precursor (SOP)  
55 divides asymmetrically to generate pIIa and pIIb cells that undergo subsequent cell  
56 divisions giving rise to the four cells composing the adult SO (Fig. 1A') (Fichelson  
57 and Gho, 2003; Gho et al., 1999; Hartenstein and Posakony, 1989). At each cell  
58 division, cell fate determinant Numb and Neuralized are unequally segregated to  
59 control Notch-dependent binary fate acquisition (Langevin et al., 2005; Le Borgne  
60 and Schweisguth, 2003; Rhyu et al., 1994). In contrast to EC, SO and daughters are  
61 fast cycling cells (Audibert, 2005) (Fig. 1A') raising the question of how permeability  
62 barrier and abscission occur during SOP cytokinesis to ensure the proper  
63 progression of cell divisions while enabling cell fate determination. In this study, we  
64 first characterized the coordination between the midbody basal displacement and the  
65 SJ remodeling during SOP cytokinesis. We next investigated the functions of Shrub  
66 and SJ components in abscission. We provided evidence that SJ components  
67 negatively regulate the timing of abscission during SOP cytokinesis. We also report

68 that Shrub, by controlling the abscission and the remodeling of SJs, exerts two  
69 complementary functions to orchestrate SO abscission.

## 70 **Results**

71

### 72 **Basal displacement of the midbody is faster in SOP than in epidermal cells**

73 To monitor SOP cell cytokinesis and compare it to that of epidermal cells (ECs), we  
74 live-imaged non-muscle Myosin II light chain tagged with RFP (MyoIIIRFP) to label  
75 the plane of AJs and the actomyosin contractile ring dynamics, ATP $\alpha$  tagged with  
76 GFP (ATP $\alpha$ GFP) to monitor the SJs (Fig. 1B-B' and Fig. S1A-A'). SOP and its  
77 pIIa/pIIb daughter cells were identified using Histone 2B::IRFP670 (H2BIR)  
78 expressed under the minimal promoter of *neuralized* (Fig. 1B-1B'). In each movie,  
79 time is expressed in min, with t0 corresponding to the onset of anaphase. In both EC  
80 and SOP, the constriction of the actomyosin contractile ring gives rise to the midbody  
81 located basal to the AJ, within the SJs (Fig. 1B-B', Fig.S1A-A' at t10 and (Daniel et  
82 al., 2018; Founounou et al., 2013; Guillot and Lecuit, 2013; Herszterg et al., 2013;  
83 Morais-de-Sá and Sunkel, 2013)). As described for dividing ECs (Fig. 1-Fig. S1A,  
84 t10 ;(Daniel et al., 2018; Wang et al., 2018)), as a result of membrane ingression  
85 induced by actomyosin ring pulling, neighboring cells remain tightly associated to  
86 SOPs by finger-like protrusions, marked with the SJs components ATP $\alpha$ GFP and  
87 Cora (Fig. 1B, t10; SJ plane, Fig. 1C-C', t10; SJ plane). While another commonality  
88 of the SOPs and ECs is the displacement of the midbody towards the basal pole  
89 (Fig. 1B', Fig. S 1A', arrows), we found that the basal displacement of the SOP  
90 midbody is 1.75 times faster ( $2.8\pm 0.1$   $\mu\text{m}/\text{h}$ ) than that of the EC ( $1.6\pm 0.1$   $\mu\text{m}/\text{h}$ ) in the  
91 80 min after anaphase onset (Fig. 1D-E). Then, we observed an inflection in the  
92 curve, the SOP midbody being displaced with a faster kinetic towards the basal side  
93 ( $6.9\pm 0.2$   $\mu\text{m}/\text{h}$ ) (Fig. 1E), as it is progressively leaving the SJ domain (Fig. 1B',  
94 between t90 and t115). As the newly assembled SJs acts as a conveyor belt that  
95 triggers the basal displacement of the midbody in ECs (Daniel et al., 2018), the  
96 difference in midbody basal displacement between EC and SOP predicts a faster SJ  
97 remodeling in SOP that we next investigated.

98

### 99 **Remodeling of SJ coincides with SOP midbody basal displacement**

100 We then follow the SJs present in the finger-like protrusions, i.e. the junctions that  
101 were present prior to entry into mitosis (Daniel et al., 2018), and discriminate the SJ  
102 components of the dividing cell from those of the neighbors. For this purpose, we  
103 generated clones of dividing EC or SOP cells expressing MyoIIIRFP and no

104 ATP $\alpha$ GFP, but expressing endogenous untagged ATP $\alpha$ , and imaged adjacent to  
105 cells expressing ATP $\alpha$ GFP and MyoIIIRFP (Fig. 2A, Fig. 2-Fig. S 2A). At t10, the  
106 presence of ATP $\alpha$ GFP signal in the finger-like protrusions pointing towards the  
107 midbody is originating from the neighbor cell, confirming that the integrity of the SJ  
108 barrier is preserved between the SOP and its neighboring EC, as we had previously  
109 described between two ECs (Fig. 2A, Fig. 2-Fig. S 2A, SJ plane and (Daniel et al.,  
110 2018)). In SOP, as the midbody underwent its basal displacement, at t70 $\pm$ 7, the  
111 finger-like protrusions thinned and both edges were no longer resolved by light  
112 microscopy (t65, Fig. 2A; SJ plane, n=4). At t97 $\pm$ 4.5, the finger-like protrusion was  
113 barely detectable (t100, Fig. 2A, SJ plane, n=5). Then, the midbody was no longer  
114 seen within the plane of the SJs (t110, Fig. 2A, and t115, Fig.1C), prior to be  
115 displaced at distance, basal to pIIa nucleus that we interpret as the release of SOP  
116 midbody (see below) (t120, Fig. 2A; see also Fig. 1C-C'). In contrast, in EC, the  
117 finger-like protrusions connected to the midbody are persisting after t120 (Fig. 1, Fig.  
118 S1A and (Daniel et al., 2018)), indicating that the disengagement of finger-like  
119 protrusions and midbody release occurs faster in SOP daughters than in ECs.  
120 We next analyzed the converse situation to monitor the *de novo* assembly of SJs at  
121 the new SOP daughter interface by live-imaging SOP expressing ATP $\alpha$ GFP  
122 surrounded by ECs expressing endogenous untagged ATP $\alpha$ . As the cell divides, we  
123 observed the appearance of an ATP $\alpha$ GFP signal apical to the midbody (t20, Fig. 2B,  
124 SJ plane) which then formed a continuous line, i.e. the novel SJ at t45 (t45, Fig. 2B,  
125 SJ plane) compared to t80 in ECs (data not shown and (Daniel et al., 2018)). These  
126 results suggest that SJ assembly is faster in SOP daughters than in EC daughters.  
127 To confirm this, we performed fluorescence recovery of ATP $\alpha$ GFP signal after  
128 photobleaching (FRAP) experiments (Fig. 2C). 40 min after photobleaching one of  
129 the two finger-like protrusions of dividing ECs, ATP $\alpha$ GFP signal was barely  
130 recovered, presenting mainly an immobile fraction ( $y_{max}$ = 17 % and a t1/2 = 7.4  
131 min, –in agreement with previous observations (Fig. 2D, (Daniel et al., 2018)). In  
132 contrast, following FRAP of the SOP daughter interface, identified with the plasma  
133 membrane marker GAP43::IRFP670, about 50% of ATP $\alpha$ GFP signal was recovered  
134 40 min at the new daughter interface above the midbody ( $y_{max}$  = 49 % and t1/2 =  
135 10.2 min, Fig. 2C; SJ plane and Fig. 2D).

136 These data show that the formation of the new SJ, the disengagement of the SJ  
137 finger-like protrusions and midbody release occur earlier in SOP daughters than in  
138 EC daughters.

139

140 **Cytoplasmic isolation and midbody release following SOP division are**  
141 **stereotyped and temporally decoupled**

142

143 In order to determine when the cytoplasm of the pIIa and pIIb cells are physically  
144 separated, we used the photoconvertible probe KAEDE as previously described  
145 (Daniel et al., 2018). When photoconverted in the pIIa (or pIIb) cell, photoconverted  
146 KAEDE is expected to freely diffuse into the pIIb (or pIIa) cell prior to cytoplasmic  
147 isolation, whereas it should be restricted to pIIa (or pIIb) cell after cytoplasmic  
148 isolation (Fig. 3-Fig. S3A and data not shown). We used *pnr-Gal4* to express KAEDE  
149 and to subsequently proceed to UAS-GAL4 driven gene silencing.

150 For each SOP, identified using GAP43IR, photoconversion of KAEDE was  
151 conducted at a specific time point after the onset of anaphase. For example, when  
152 photoconversion was performed in the pIIa 61 min after the onset of anaphase, the  
153 photo-converted probe diffused into the pIIb cell (Fig. 3A-A'). By contrast, when  
154 photoconversion was performed 63 min post anaphase onset, KAEDE remained  
155 restricted in the pIIa cell indicating that cytoplasmic isolation had occurred (Fig. 3B-  
156 B'). This experiment was repeated over several time points ranging from 46 to 71  
157 min (Fig. 3-Fig. S3B), and the result of each individual experiment, i.e. KAEDE able  
158 to diffuse or not, were modeled via logistic regression, using the generalized linear  
159 model (GLM) (Fig. 3C, see method section). The proportion of cells exhibiting  
160 cytoplasmic isolation increased as function of time (Fig. 3C). In our study, due to  
161 lethality with the *pnr-Gal4* driver in one of our conditions, we had to use *scabrous*  
162 (*sca-GAL4* (Mlodzik et al., 1990)). As in the control *pnr-GAL4* line, we noticed that  
163 proportion of cells exhibiting cytoplasmic isolation increased as function of time, but  
164 a delay was observed (Fig. 3-Fig. S3B-C and analysis of deviance Table S1A). We  
165 estimated the time at which 50% of the pIIa/pIIb cell indicated cytoplasmic isolation  
166 (herein termed  $t_{1/2}$ , see method section) and determined that  $t_{1/2}$  are  $58.9 \pm 1.14$  min  
167 and  $66.54 \pm 1.36$  min for *pnr-Gal4* and *sca-Gal4* respectively. The reason for the  $t_{1/2}$   
168 difference is unknown between the two conditions and is probably related to the  
169 genetic background. For the sake of simplicity in the comparison of effect of gene

170 silencing (see below), since both Gal4 driver lines were used as control values, we  
171 arbitrary set the t1/2 of control *pnr*-Gal4 and control *sca*-Gal4 to a relative time  
172 centered to 0.

173

174 To determine if the cytoplasmic isolation is coupled to the physical cut and release of  
175 the midbody, we next monitored the position of the midbody relative to the plasma  
176 membrane of the SOP daughter cells, we imaged MyoII<sup>GFP</sup> together with the  
177 membrane marker GAP43IR (Fig. 3D). 10 min after anaphase onset, the midbody  
178 colocalized with GAP43IR at the pIIa-pIIb daughter cells interface (t10, Fig. 3D, MB  
179 level) and remained at the pIIa-pIIb interface until t100 (t100, Fig. 3A, MB level). At  
180 t105, the midbody leaves the pIIa-pIIb daughter membrane interface (Fig. 3D, MB  
181 level,  $110.8 \pm 12.9$  min, n=12), just prior to or concomitant with the pIIb cell anaphase  
182 onset ( $123.4 \pm 6.9$  min, n=13). After its departure from the pIIa-pIIb interface, the  
183 midbody is mainly inherited by the pIIa cell (t105, t110, Fig. 3D, MB level, 91% of the  
184 cases, n=11) where it remains attached to the plasma membrane (Fig. 3D') before  
185 the MyoII<sup>GFP</sup> signals becomes undetected in pIIa/pIIb cells at t115 (Fig. 3D,  
186  $121.5 \pm 14$  min, n=13). Based on the Fig. 3D, we illustrated the midbody displacement  
187 at the pIIa membrane at each time point (Fig. 3D''). In isolated cells, midbodies can  
188 be internalized/phagocytosed in acidic intracellular compartments following  
189 abscission (Crowell et al., 2014). To test if the loss of MyoII<sup>GFP</sup> signal reflects the  
190 loss of GFP signal due to signal quenching by low endosomal pH (Couturier et al.,  
191 2014) or the physical disappearance of the midbody, we co-imaged MyoII<sup>RFP</sup> and  
192 MyoII<sup>GFP</sup> together with GAP43IR (Fig. 3-Fig. S3D). Both signals disappeared  
193 simultaneously from the pIIa cell and are found outside of the daughter cells at t0  
194 with some GAP43IR signal (Fig. 3-Fig. S3D-D'). We also live-imaged the kinesin-like  
195 protein Pavarotti (Pav<sup>GFP</sup>), a member of the centralsplindin complex, together with  
196 MyoII<sup>RFP</sup> and GAP43IR (Fig. 3-Fig. S3E) and observed that Pav<sup>GFP</sup> and MyoII<sup>RFP</sup>  
197 signals disappeared simultaneously outside of the daughter cells at t0 with some  
198 GAP43IR signal (Fig. 3-Fig. S3E-E'). These data argue that the midbody is not  
199 internalized/phagocytosed in the pIIa cell. Instead, the midbody was found at  
200 distance from the pIIa cell and was still marked by the GFP, RFP markers as well as  
201 the plasma membrane marker GAP43IR indicating that it was in the extracellular  
202 space, not in endocytic compartments of epidermal cells (Fig. 3-Fig. S3D', S3E').

203

204 The sequence of cytoplasmic isolation, the formation of the new bSJs, the  
205 disengagement of the SJ finger-like protrusions, and the midbody release in SOP are  
206 depicted on a chronological timeline (Fig. 3E). Having described the events and  
207 established the timeline, we next investigated the molecular mechanisms underlying  
208 epithelial cell abscission of SOP daughters.

209

### 210 **ESCRT III/Shrub localizes at the midbody and in the finger-like protrusions**

211 Based on the evolutionarily conserved function of ESCRT-III/CHMP4B in abscission  
212 from archaia to vertebrates, we investigated Shrub function in SOP abscission. We  
213 first monitored the localization of Shrub. Because available anti-Shrub antibodies  
214 give no obvious membrane associated signal following chemical fixation (data not  
215 shown; (Pannen et al., 2020)), we made use of a GFP tagged version of Shrub  
216 engineered by CRISPR/Cas9 (ShrubGFP, (Mathieu et al., 2022)). We then live-  
217 imaged MyoRFP and ShrubGFP (Fig. 4A). t30-60 after the onset of anaphase, a  
218 faint signal of ShrubGFP is detected in the plane of the midbody and is slightly  
219 enriched along the new daughter cell interface/finger-like protrusion (Fig. 4A', and  
220 4A''). At  $t70 \pm 10$ , while the intensity of the ShrubGFP signal along the pIIa-pIIb  
221 interface/finger-like protrusions decreased, ShrubGFP signal was detected in the  
222 form of two punctae, one on each side of the midbody, a signal that was still present  
223 at t120 (Fig. 4A', 4A''', n=16).

224

225 To determine if the ShrubGFP signal adjacent to the midbody was coming from the  
226 SOP, the neighbors or both (Fig. 4A'), we imaged clones of SOP and EC dividing  
227 cells expressing MyoIIIRFP devoid of ShrubGFP close to cells expressing ShrubGFP  
228 under the *Ay-Gal4* system (Fig. 4B, Fig. 4-Fig. S4A). A ShrubGFP-positive punctum  
229 emanating from the non-dividing neighboring cell was detected at the tip of the  
230 finger-like protrusion pointing to the midbody of the SOP (from t18 to t72, Fig. 4B  
231 and t36, Fig. 4B') or to the midbody of the EC (Fig. 4-Fig. S 4A and t36 Fig. 4-Fig.  
232 S4A'). In the converse situation in which clones of SOP dividing cells expressing  
233 ShrubGFP were close to cells devoid of ShrubGFP (Fig. 4C), at t26 a first punctum  
234 of ShrubGFP was appearing at the midbody before the appearance of a second  
235 punctum at t60 (Fig. 4C and Fig. 4C'). At t90, the punctae were still present on both  
236 side of the midbody of the SOPs (Fig. 4C). In EC, a punctum is detected on one side  
237 of the midbody from t28 to t90 (Fig. 4-Fig. S4B and t60 Fig. 4-Fig. S4B'). In contrast

238 to SOPs, we never observed punctae of ShrubGFP on each side of the midbody in  
239 the EC. These data revealed the existence of two pools of Shrub, one in the finger-  
240 like protrusion and one at the midbody of the SOP, calling for two distinct functions of  
241 Shrub.

242

### 243 **Shrub regulates the timing of cytoplasmic isolation of SOP daughter cells**

244 Based on the localization of ShrubGFP at the midbody, we next investigated if Shrub  
245 was involved in the abscission by interfering with Shrub function. However, Shrub is  
246 required in several processes making difficult to analyze its function. Indeed, clones  
247 of epithelial cells homozygous mutant for a null allele of *Shrub*<sup>G5</sup> delaminate even  
248 when apoptosis was suppressed by p35 expression (Hay et al., 1994), preventing us  
249 from analyzing abscission in *Shrub* homozygote mutant cells. To circumvent this  
250 problem, we opted for an UAS/Gal4-based tissue inducible-based RNAi approach  
251 using *sca*-GAL4. We report that silencing of Shrub, in areas where shrub is highly  
252 depleted, caused the enlargement of HRS-positive endosomes (Fig. 4- Fig. S4C),  
253 the accumulation of Crumbs in endocytic compartments as reported in the  
254 *Drosophila* trachea (Dong et al., 2014), and the accumulation of the Claudin-like  
255 Kune Kune in intracellular compartments (Fig. 4D) as reported for other claudin-like  
256 proteins (Pannen et al., 2020), NrXIV as well as sinuous (Fig. 4-Fig. S4D-E). These  
257 three phenotypes are characteristic by the impact of loss of ESCRT-III on  
258 intracellular trafficking (Dong et al., 2014; Vaccari et al., 2009), attesting to the  
259 effectiveness of the silencing approach. We next determined the consequence of  
260 Shrub depletion on the timing of cytoplasmic isolation using the KAEDE  
261 photoconversion assay. We performed our experiments in areas in which KAEDE is  
262 expressed only in SOP and daughters. In this part of the notum, this mild depletion of  
263 shrub does not noticeably affect the distribution of SJ components (data not shown).  
264 We found that SOP-specific silencing of Shrub caused a delay in cytoplasmic  
265 isolation (Fig. 4E, with a t1/2 delayed of 5.9±1.4 min compared to the *sca* control and  
266 Table S1B) indicating that Shrub regulates the timing of cytoplasmic isolation. This  
267 data identifies a cell-autonomous function of Shrub in abscission.

268 We also observed that ShrubGFP is a mutant allele of Shrub, causing a delay in  
269 abscission in the female germline stem cyst of *Drosophila* heterozygote for  
270 ShrubGFP (67/ 181 GSC with delayed abscission, Fig. 5-Fig. S5A). Similarly in the  
271 notum, we observe that the presence of one copy of ShrubGFP delayed the timing of

272 cytoplasmic isolation (Fig. 5,  $t_{1/2} +10.3\pm 1.4$  min compared to *pnr* control, Table  
273 S1C). This delay in abscission observed with *shrubGFP* is also likely to explain the  
274 delay between the detection of two punctae of *ShrubGFP* at the midbody (Fig. 4A',  
275  $t=70\pm 10$  min) and the timing of abscission measured in control cells devoid of  
276 *ShrubGFP* (Fig. 3E,  $t_{1/2}= 58.9\pm 1.1$ min). Although *ShrubGFP* is an allele of *Shrub*,  
277 *ShrubGFP* signal observed on both sides of the midbody is specific as *CHMP2BGFP*  
278 (charged multi vesicular body protein 2b tagged GFP), another ESCRT-III  
279 component recruited in a *Shrub* dependent manner (Babst et al., 2002), exhibits a  
280 similar localization pattern (Fig. 5-Fig. S5B). We conclude that *Shrub* is recruited in a  
281 cell autonomous manner on both side of the SOP midbody to control cytoplasmic  
282 isolation.

283

#### 284 **Coordination between bSJs assembly and timing of abscission**

285 The fact that *Shrub* is recruited in the finger-like protrusion at a location where SJ  
286 remodeling is taking place, and the fact that *Shrub* depletion has an impact on the  
287 integrity of the SJs, prompted us to next investigate whether SJ components could  
288 influence the timing of cytoplasmic isolation. We found that depletion of *Cora* in the  
289 SOP and the ECS causes a premature cytoplasmic isolation (Fig. 6A, B; with a  $t_{1/2} -$   
290  $5.8\pm 1.7$  min compared to  $t_{1/2}$  *pnr* reference control and Table S1C). We also  
291 tracked the position of the midbody upon *Cora* depletion by live-imaging *MyoII*GFP  
292 together with *GAP43IR* (Fig. 6C). 10 min after anaphase onset, the midbody co-  
293 localized with *GAP43IR* at the interface between the two daughter cells ( $t_{10}$ , MB  
294 level, Fig. 6C). Then, the midbody is released from the interface at  $t_{70}$  (Fig. 6C, MB  
295 level,  $88.7\pm 14.8$  min,  $n=8$ ) and is not detected within the *pIIa* cell at  $t_{85}$  (Fig. 6C,  
296  $94.3\pm 11.3$  min,  $n=7$ ). Thus, the midbody release and its disappearance from the *pIIa*  
297 cell happen earlier than in the control (Fig. 6D and 6E respectively). This is not  
298 caused by an acceleration of cell cycle in *Cora* depleted cells as the entry into  
299 anaphase onset of *pIIb* and *pIIa* takes place later compared to the control (Fig. 6F).  
300 Together, these data shows that abscission happens earlier upon *Cora* depletion  
301 than in the control and indicates that the formation of SJs delays abscission timing of  
302 the SOP.

303 Thus, *Shrub* and the SJ component *Cora* act as positive and negative regulators of  
304 cytoplasmic isolation of SOP daughters, respectively. However, because depletion of  
305 *Shrub* leads to altered localization of SJ components ((Pannen et al., 2020); Fig. 4D

306 and - Fig. S4D-E) the above results are counterintuitive at a first glance. Indeed, in a  
307 simplistic model in which Shrub would only be required for SJ remodeling, depletion  
308 of Shrub by causing a reduction in the amounts of SJ components should lead to  
309 early cytoplasmic isolation. Nevertheless, as indicated above, Shrub also localizes at  
310 the midbody level where it promotes abscission. These data on the dual function of  
311 Shrub led us to further study the relationship between Shrub and Cora. Silencing of  
312 Cora caused an increased recruitment of ShrubGFP within the finger-like protrusion  
313 in one third of the cases, (n=6; Fig. 6G', t30-t70 and Fig. 6H) further suggesting a  
314 function for Shrub at the site of local SJ remodeling (see discussion). Because,  
315 ShrubGFP behaves like a mutant allele delaying abscission (Fig. 5E), we reasoned  
316 that the presence of ShrubGFP could modify the timing of abscission measured  
317 upon simple depletion of Cora. The timing of cytoplasmic isolation upon Cora  
318 depletion in the presence of ShrubGFP mutant allele caused a premature isolation  
319 compared to ShrubGFP allele alone (t<sub>1/2</sub> difference of 12.1 min). Plotting results  
320 also suggest a tendency for Cora depleted cells to exhibit greater proportions of a  
321 premature cytoplasmic isolation than when shrubGFP allele is expressed in Cora  
322 depleted cells (t<sub>1/2</sub> difference of 4.09 min).

323 Overall, these data indicate that Shrub exerts two functions during SOP cytokinesis:  
324 a first function, at the level of the SOP midbody to control the timing of cytoplasmic  
325 isolation; and a second cell non-autonomous function in the finger-like protrusions for  
326 the SJ-based remodeling (Fig. 6I).

327

## 328 **Discussion**

329 In this study, we further characterized the coordination of abscission and the  
330 maintenance of epithelial permeability barrier functions during cytokinesis in dividing  
331 SOPs and compared them to symmetrically dividing epidermal cells. In both types of  
332 cells, the midbody assembles below the newly forming pIIa-pIIb adherens junctions.  
333 In the plane of the midbody, the neighboring cells remains in contact with the divided  
334 cell through finger-like protrusions. These finger-like protrusions are located within  
335 the layer of SJs that were already connecting the neighbors and the SOP prior to  
336 SOP mitosis. The disassembly of SJs appears to be the rate limiting step for the  
337 disentangling of the finger-like protrusions. We reported that the basal displacement  
338 of the midbody and the *de novo* assembly of SJs occurs faster in SOP than in EC,  
339 resulting in a quicker disentanglement of the finger-like protrusions, an event that

340 precedes midbody release. We have described that cytoplasmic isolation is  
341 temporally uncoupled to midbody release, suggesting that abscission is a two-step  
342 process. At the molecular level, SJ components negatively regulate the timing of  
343 cytoplasmic isolation implying a regulatory role of permeability barrier maintenance  
344 on abscission. Finally, we reported that Shrub exerts two complementary functions in  
345 SOP abscission. A first, cell autonomous control of the timing of cytoplasmic isolation  
346 at the level of the SOP midbody. The second function of Shrub is at the finger-like  
347 protrusions to remodel SJs and prevent premature abscission until the permeability  
348 barrier is fully assembled.

349

### 350 **Dynamics of bSJs assembly and midbody release in SOP compared to EC**

351 FRAP analyses revealed that the percentage of mobile fraction of ATP $\alpha$ GFP is  
352 increased in SOPs compared to ECs, suggesting that the assembly of SJs at the  
353 new pIIa-pIIb interface occurs faster in SOPs. In addition, the disentanglement of the  
354 finger-like protrusions, corresponding to the completion of disassembly of SJs  
355 between SOP and neighbors also occurs faster in SOPs. This is associated with a  
356 faster basal displacement of the midbody. These results add arguments in favor of  
357 the concept that *de novo* assembly of SJs acts as a conveyor belt of midbody basal  
358 displacement (Daniel et al., 2018). As the endosomal system actively contributes to  
359 transport and turnover of SJ complexes (Nilton et al., 2010; Pannen et al., 2020;  
360 Tempesta et al., 2017; Tiklová et al., 2010), our data suggest some differences in the  
361 intracellular trafficking between SOP and EC. As SOP daughters enter into mitosis  
362 about 90-120 min after the anaphase onset of SOP division, the dynamics of  
363 membrane trafficking might be under cell cycle regulation. It is also possible that the  
364 transcriptional program of SOPs includes specific membrane trafficking regulators or  
365 SJ components that directly impact the kinetics of assembly of SJs. In addition, as  
366 the disentanglement of the finger-like protrusions occurs faster in SOPs, our data  
367 also implies that the dynamic of assembly and disassembly of SJs in the SOPs and  
368 its daughters dictates the dynamics of SJ components in the neighboring ECs. Thus,  
369 the dynamics of SJ between ECs and SOPs is different than between two ECs.

370

### 371 **Role of SJ components in regulating SOP cytoplasmic isolation**

372 We report that loss of SJ components results in premature cytoplasmic isolation,  
373 raising the question of how can SJ components negatively regulate abscission? In

374 the finger-like protrusions formed as the result of cytokinetic ring constriction, the  
375 nascent midbody is embedded in the SJs that were assembled between the SOP  
376 and its EC neighbors prior to mitosis. This topology ensures that at the level of the  
377 midbody within the finger-like protrusion, the permeability barrier function is  
378 maintained. Above the midbody, the novel SJ between SOP daughters then  
379 progressively assembles to build the permeability barrier between the daughters. We  
380 envision the topology of the finger-like protrusions as a mean of maintaining the  
381 mother-daughter permeability barrier throughout cytokinesis. The disentanglement of  
382 finger-like protrusions corresponds to the dismantlement of the old SJ leading to the  
383 release of the midbody. Thus, apical to basal displacement of the finger-like  
384 protrusions involves intense membrane remodeling and probably membrane  
385 trafficking which include Shrub-dependent trafficking. Upon Depletion of Cora, Shrub  
386 is found at higher levels in the finger-like protrusions, and the process leading to  
387 abscission and midbody release is accelerated. While the molecular trigger is yet to  
388 be characterized, a simple possibility is that SJ components negatively regulate  
389 Shrub recruitment at the level of the midbody and in the finger-like protrusions.

390

### 391 **Temporal uncoupling between cytoplasmic isolation and midbody release**

392 In isolated vertebrate cells, the cytoplasmic isolation is concomitant with abscission,  
393 i.e. the physical separation of the divided cells (Guizetti et al., 2011; Steigemann et  
394 al., 2009). We showed here, as demonstrated in the *C. elegans* one cell embryo  
395 (Green et al., 2013), that cytoplasmic isolation and midbody release are temporally  
396 separated events (Fig. 3F). A possible caveat in our study resides in the use of the  
397 KAEDE probe, a 116kDa homotetramer (Ando et al., 2002). Indeed, we cannot  
398 exclude that a probe of smaller size or a solute would still be able to equilibrate after  
399 the time we have here determined as the timing of cytoplasmic isolation. However,  
400 the fact that Shrub is recruited on both side of the midbody and regulates the time  
401 when the KAEDE probe is no longer able to diffuse between the divided cells argues  
402 that cytoplasmic isolation occurs several minutes prior to midbody release. As the  
403 midbody release coincide with the disentanglement of the finger-like protrusions (Fig.  
404 3F), we propose that the midbody is embedded within the SJ strands and released  
405 only upon SJ disassembly. Following its release from the pIIa-pIIb interface, the  
406 midbody is displaced on the surface of the pIIa cell until it detaches and found at  
407 distance from the pIIa cell. There, the midbody is still labelled with

408 MyoIIIGFP/PavGFP, MyoIIRFP and GAP43IR markers suggesting that the midbody  
409 is in the extracellular space rather than being internalized by adjacent epidermal  
410 cells.

411

#### 412 **Cell autonomous and cell non-autonomous functions of Shrub**

413 We report that Shrub positively and cell autonomously regulates abscission in SOP  
414 as also observed in mammalian cultured cells and *Drosophila* germline stem cell  
415 (Eikenes et al., 2015; Matias et al., 2015). ShrubGFP appears in the form of  
416 punctiform signal in a stereotyped manner on both sides of the SOP midbody. These  
417 two puncta of ShrubGFP are recruited at the midbody long before the midbody  
418 release. This is also observed in female *Drosophila* germline stem cells where Shrub  
419 is recruited to the ring canal from G1/S prior to abscission in G2 phase of the  
420 following cell cycle (Eikenes et al., 2015; Matias et al., 2015). Interestingly,  
421 recruitment of Shrub occurs around the S to G2 transition of the daughter cells and  
422 about one hour after the entry of SOP into mitosis (Audibert, 2005). Then, the  
423 midbody release takes place just before the G2/M transition of the pIIb cell. Thus, the  
424 temporal regulation of abscission in SOP appears to follow a similar cell-cycle  
425 dependent regulation as the *Drosophila* germline stem cells. Whether this cell-cycle  
426 dependence is specific to stem cells and progenitors or also applies to epidermal  
427 cells await further investigation.

428 Another pool of Shrub is acting in a cell non-autonomous manner. As in SOPs,  
429 ShrubGFP is also recruited at the midbody of the dividing epidermal cell and is  
430 recruited in the finger-like protrusions. What could be the function of the pool of  
431 ShrubGFP in the finger-like protrusions? Based on the fact that Shrub regulates SJs  
432 steady state distribution and dynamics (Pannen et al., 2020), and is also known to  
433 regulate endosomal sorting, Shrub could locally participate in SJ remodeling.  
434 Alternatively, based on the geometry of the tip of the finger-like protrusions and  
435 possible local constraints linked to basal displacement of the SOP midbody, Shrub  
436 could be recruited there to promote membrane repair (Jimenez et al., 2014; Scheffer  
437 et al., 2014) and/or locally compensate for leakage in permeability barrier function.  
438 Consistent with this model, when the permeability barrier function is challenged, as  
439 for example during Cora depletion, ShrubGFP is prone to accumulate in the finger-  
440 like protrusions.

441

442 **Abscission timing, midbody inheritance and cell fate decision**

443 A link between the regulation of cell division and fate decision is reported and  
444 abscission is thought to regulate fate acquisition (Chaigne et al., 2020; Ettinger et al.,  
445 2011). Here, we found that the abscission is asymmetric with the midbody remnant  
446 inherited by the pIIa cell in most cases. By analogy with the *C. elegans* single-cell  
447 embryo, the midbody could be inherited by default by the cell that will divide later  
448 than its daughter (Green et al., 2013). Can SOP midbody remnant signal and impact  
449 on proliferation, differentiation and/or cell fate as in mammalian cells (Ettinger et al.,  
450 2011; Kuo et al., 2011; Peterman et al., 2019; Pohl and Jentsch, 2009) ? Whether  
451 SOP midbody exerts a function on proliferation awaits further monitoring of its  
452 behavior (uptake?) after its release from the pIIa cell.

453

454 The fact that abscission occurs rather late after the anaphase onset while Notch-  
455 dependent fate acquisition is initiated about 15 min after the onset of anaphase  
456 raises an intriguing question (Bellec et al., 2018; Couturier et al., 2012). Indeed, our  
457 photo-activation experiment shows that pIIa and pIIb share their cytoplasm until t60  
458 after anaphase, which contrasts with the fact that the Notch intracellular domain  
459 (NICD) is translocated exclusively in the nucleus of pIIa . The cell fate determinants  
460 Numb and Neuralized, two cytosolic proteins, are also unequally inherited by the pIIb  
461 cell before cytoplasmic isolation. An interesting question is how NICD, and Numb,  
462 Neuralized remain confined to pIIa and pIIb cells respectively, while at the same time  
463 the KAEDE probe freely diffuses bidirectionally. This situation is reminiscent to that  
464 of phospho-Mad that remains restricted to the most anterior of *Drosophila* germline  
465 stem cells in stem cysts (Eikenes et al., 2015; Mathieu et al., 2013; Matias et al.,  
466 2015). Unless, Notch signaling components are assembled in very large protein  
467 complexes or with cytoskeletal components that prevent them from diffusing through  
468 the opened intercellular bridge, these data imply that selective passage must be  
469 regulated at the intercellular bridge (Mullins and Biesele, 1977; Norden et al., 2006;  
470 Steigemann et al., 2009), as reported for proteins and organelles in yeast (Lengefeld  
471 and Barral, 2018).

472

473 Overall, our study sheds light on a complex coordination of abscission, maintenance  
474 of epithelial permeability barrier functions and fate acquisition in SOPs. Based on the  
475 apico-basal topology of mechanical and permeability barriers, apical positioning of

476 the midbody within the tight junctions in vertebrates (Dubreuil et al., 2007; Higashi et  
477 al., 2016; Jinguji and Ishikawa, 1992) and the role of ESCRT components in tight  
478 junction protein trafficking (Dukes et al., 2011; Raiborg and Stenmark, 2009), it is  
479 tempting to speculate that the cell autonomous and non-autonomous effects we  
480 described in this study may also be at play during epithelial abscission of progenitors  
481 in vertebrates.

482

483

#### 484 **Acknowledgements**

485 We thank Vanessa Auld, Anne Uv, the Bloomington Stock Center, the Vienna  
486 *Drosophila* RNAi Center and the National Institute of Genetics Fly Stock Center for  
487 providing fly stocks. We also thank S. Dutertre and X. Pinson from the Microscopy  
488 Rennes Imaging Center-BIOSIT (France). The monoclonal antibodies against Elav,  
489 Cut, Cora, DE-Cad and  $\alpha$ -spectrin were obtained from the Developmental Studies  
490 Hybridoma Bank, generated under the auspices of the National Institute of Child  
491 Health and Human Development, and maintained by the University of Iowa  
492 Department of Biological Sciences. We thank Arnaud Echard, Thomas Esmangart  
493 de Bournonville, and members of RLB's lab for critical reading of the manuscript. We  
494 also thank R.J. Scott Mc Cairns for the help with the GLM models.

495

#### 496 **Competing interests**

497 The authors declare no competing or financial interests.

498

#### 499 **Author contributions**

500

#### 501 **Funding**

502 This work was supported in part by the La Ligue contre le Cancer-Equipe Labellisée  
503 (R.L.B.) and the Association Nationale de la Recherche et de la Technologie  
504 programme PRC Vie, santé et bien-être CytoSIGN (ANR-16-CE13-004-01 to R.L.B.).

505

506

507 **Materials and Methods**

508 **Key resources table**

REAGENT OR RESOURCES	SOURCE	IDENTIFIER
Antibodies		
Mouse anti-Coracle (1:200)	DSHB	C615.16
Rabbit anti- Kune Kune (1:1500)	Kind gift from Mikio Furuse (Nelson et al., 2010)	N/A
Rabbit anti-NrxIV (1:1000)	(Stork et al., 2009)	N/A
Rabbit anti Sinuous (1:1000)	Kind gift from Dr. Greg Beitel (Wu et al., 2004)	N/A
mouse-anti- $\alpha$ -spectrin (1:500)	DSHB	Clone 1A9
Rat anti-Crumbs (1:1000)	Kind gift from Elisabeth Knust (Richard et al., 2006)	N/A
Rat anti-DE-cad (1:250)	DSHB	DCAD2
Mouse anti-HRS (1:200)	DSHB	Clone 27-4
Cy2, Cy3 or Cy5-coupled secondary antibodies (1:300)	The Jackson laboratory	N/A
Chemicals		
Hoechst	Thermofischer	62249
CityFluor	Agar scientific	AGR1320
DABCO	Sigma	S8032
N-Propyl-Gallate	Sigma	200-289-5
Paraformaldéhyde	EMS	19340-72
Phosphate Buffer Saline	Lonza	BE17-515F
Triton X-100	Euromedex	2000 B
Voltalef 10S	VWR	24627.188

REAGENT OR RESOURCES	SOURCE	IDENTIFIER
Experimental models: Organisms/ Strain		
<i>D. melanogaster</i> : w <sup>1118</sup>	BDSC	BL3605
<i>D. melanogaster</i> . MyoII::RFP <sup>crispr</sup>	(Daniel et al., 2018)	N/A
<i>D. melanogaster</i> . MyoII::GFP <sup>crispr</sup>	(Esmangart de Bournonville and Le Borgne, 2020)	N/A
<i>D. melanogaster</i> . Shrub::GFP <sup>crispr</sup> /CyO	(Mathieu et al., 2022)	N/A
<i>D. melanogaster</i> . CHMP2B::GFP <sup>crispr</sup> /CyO	(Mathieu et al., 2022)	N/A
<i>D. melanogaster</i> . Pavarotti::GFP	inDroso	N/A
<i>D. melanogaster</i> . ATPα::GFP/TM6, Sb, Tb	BDSC	BL59297
<i>D. melanogaster</i> . FRT82B ATPα::GFP/TM6, Tb	(Daniel et al., 2018)	N/A
<i>D. melanogaster</i> . <i>hs-FLP</i> ;; FRT82B nls::RFP	BDSC	BL30555
<i>D. melanogaster</i> . ;;MyoII-MyoII::mcherry	(Martin et al., 2009)	N/A
<i>D. melanogaster</i> . UAS-Shrub RNAi	BDSC	BL38305
<i>D. melanogaster</i> . UAS-KAEDE	BDSC	BL26161
<i>D. melanogaster</i> . UAS-KAEDE	BDSC	BL38622
<i>D. melanogaster</i> . UAS-Shrub::GFP	(Sweeney et al., 2006)	N/A
<i>D. melanogaster</i> . UAS-Cora RNAi	VDRC	9788
<i>D. melanogaster</i> . <i>neur</i> -H2B::IR	(Houssin et al., 2021)	N/A
<i>D. melanogaster</i> . <i>neur</i> -GAP43::IR	(Houssin et al., 2021)	N/A
<i>D. melanogaster</i> . <i>pnr</i> -Gal4/ TM6, Tb	(Calleja et al., 1996)	N/A
<i>D. melanogaster</i> . <i>neur</i> -GAP43::IR, <i>pnr</i> -Gal4/TM6, Tb	(Houssin et al., 2021)	N/A

REAGENT OR RESOURCES	SOURCE	IDENTIFIER
<i>D. melanogaster</i> : Ay-Gal4/Cyo	BDSC	BL3953
<i>D. melanogaster</i> : sca-Gal4	(Mlodzik et al., 1990)	N/A
Software and Algorithms		
Photoshop CS4		N/A
EasyFRAP-web	Open Source Program	N/A
Image J / FIJI	Open Source Java	N/A
Prism 8	GraphPad Version 8	N/A
R version 4.2.1	(R Core Team, 2022)	<a href="https://www.r-project.org/">https://www.r-project.org/</a>
Others		
Microscopes confocaux	Leica LSM TCS	SP8, SP5 and SPE

509  
510  
511  
512  
513  
514  
515

## 516 ***Drosophila* stocks and genetics**

517 *Drosophila melanogaster* stocks were maintained and crossed at 25°C.

518 Somatic clones were induced using the *hs-FLP* with two heat shocks (60 min at  
519 37°C) at second and third instar larvae. *pnr-Gal4* was used to drive the expression of  
520 UAS-Cora RNAi and the photoconvertible probe UAS-KAEDE. *Ay-Gal4* was used to  
521 drive the expression of UAS-ShrubGFP. *sca-Gal4* was used to drive the expression  
522 of UAS-ShrubRNAi and UAS-KAEDE.

523 Declaration of contained use of genetically modified organisms (GMOs) of  
524 containment class n°2898 from the French Ministère de l'Enseignement Supérieur,  
525 de la Recherche et de l'Innovation.

526

527 ***Drosophila* genotypes**

528

529 **Fig. 1**

530 (B) Myoll::RFP ; *neur-H2B::IR/+* ; ATP $\alpha$ ::GFP/+

531 (C-C') *neur-H2B::IR*

532 (E) Myoll::RFP ; *neur-H2B::IR/+* (EC and SOP) and Myoll::RFP ; *neur-H2B::IR/+* ;

533 ATP $\alpha$ ::GFP/+ (EC and SOP)

534

535 **Fig. 2**

536 (A-B) *hs-FLP/Myoll::RFP* ; *neur-H2B::IR/+* ; FRT82B ATP $\alpha$ ::GFP/FRT82B nls::RFP

537 (C-D) Myoll::RFP ;; ATP $\alpha$ ::GFP/*neur-GAP43::IR*

538

539 **Fig. 3**

540 (A-C) UAS::KAEDE; *neur-GAP43::IR*, *pnr-Gal4/+*

541 (D-D') Myoll::GFP, *neur-H2B*::; *neur-GAP43::IR*, *pnr-Gal4/+*

542

543 **Fig. 4**

544 (A-A') Myoll::RFP ; Shrub::GFP/+; *neur-GAP43*, *pnr-Gal4::IR/+*

545 (B-C) *hs-FLP*; UAS-Shrub::GFP/*Ay-Gal4*; *MyoII-MyoII::mcherry*

546 (D) *sca-Gal4/UAS-Shrub-RNAi*; UAS-KAEDE/+

547 (E) *sca-Gal4/UAS-Shrub-RNAi*; UAS-KAEDE/+, *sca-Gal4/UAS-Shrub-RNAi*; UAS-

548 KAEDE/*neur-GAP43::IR* and *sca-Gal4/+*; UAS-KAEDE/+

549

550 **Fig. 5**

551 UAS::KAEDE; *neur-GAP43::IR*, *pnr-Gal4/+* and UAS::KAEDE/ShrubGFP; *neur-*

552 *GAP43::IR*, *pnr-Gal4/+*

553

554 **Fig. 6**

555 (A) UAS-KAEDE/+; *neur-GAP43::IR*, *pnr-Gal4/UAS-Cora RNAi*

556 (B) UAS-KAEDE/+; *neur-GAP43::IR*, *pnr-Gal4/+* and UAS-KAEDE/+; *neur-*

557 *GAP43::IR*, *pnr-Gal4/UAS-Cora RNAi* and UAS-KAEDE/Shrub::GFP; *neur-*

558 *GAP43::IR*, *pnr-Gal4/+* and UAS-KAEDE/Shrub::GFP; *neur-GAP43::IR*, *pnr-*

559 *Gal4/UAS-CoraRNAi*

560 (C) Myoll::GFP, *neur-H2B*::; *neur-GAP43::IR*, *pnr-Gal4/ UAS::Cora RNAi*

561 (D-F) Myoll::GFP, *neur*-H2B;; *neur*-GAP43::IR, *pnr*-Gal4/+ and Myoll::GFP, *neur*-  
562 H2B;; *neur*-GAP43::IR, *pnr*-Gal4/ UAS::Cora RNAi

563 (G-G') Myoll::RFP; *shrub*GFP/+; *neur*-GAP43::IR, *pnr*-Gal4/ UAS::Cora RNAi

564

565 **Fig. S 1**

566 (A) Myoll::RFP ; *neur*-H2B::IR/+ ; ATP $\alpha$ ::GFP/+

567

568 **Fig. S 2**

569 (A) *hs*-FLP/Myoll::RFP ; *neur*-H2B::IR/+ ; FRT82B ATP $\alpha$ ::GFP/FRT82B *nls*::RFP

570

571 **Fig. S 3**

572 (B) UAS::KAEDE; *neur*-GAP43::IR, *pnr*-Gal4/+ and *sca*-Gal4/+; UAS-KAEDE/+

573 (C) UAS::KAEDE; *neur*-GAP43::IR, *pnr*-Gal4/+ and *sca*-Gal4/+; UAS-KAEDE/+

574 (E) Myoll::RFP/Myoll::GFP;; GAP43::IR/+

575 (F) Myoll::RFP;; GAP43::IR/ Pav::GFP

576

577 **Fig. S 4**

578 (A,B) *hs*-FLP; UAS-Shrub::GFP/*Ay*-Gal4; *MyoII*-Myoll::mcherry

579 (C-E) *sca*-Gal4/UAS-Shrub-RNAi; UAS-KAEDE/+

580

581 **Fig. S 5**

582 (A) *w*<sup>1118</sup> and Shrb::GFP/+

583 (B) Myoll::RFP ; CHMP2BGFP/+ ; *neur*-GAP43/+

584

585

586 **Methods**

587

588 **Immunofluorescence**

589 Pupae aged from 16 to 24h after puparium formation (APF) were dissected using  
590 Cannas microscissors in 1X Phosphate-Buffered Saline (1X PBS, pH 7.4) and fixed  
591 15 min in 4% paraformaldehyde solution at room temperature (RT) (Gho et al.,  
592 1996). Following fixation, dissected nota were permeabilized using 0.1% Triton X-  
593 100 in 1X PBS (PBT) and incubated with primary antibodies diluted in PBT for 2  
594 hours at RT. After 3 washes of 5 minutes in PBT, nota were incubated with

595 secondary antibodies diluted in PBT for 1 hour at RT. Following incubation, nota  
596 were washed 3 times in PBT, and once in PBS prior mounting in 0,5% N-  
597 propylgallate with DABCO dissolved in 1X PBS/90% glycerol.

598 For *Drosophila* germline stem cell identification, antibody staining and Hoechst  
599 staining were performed according to standard protocols. Briefly, ovaries or testis  
600 were dissected in PBS, fixed in 4% PFA, rinsed and permeabilized in PBT (PBS-  
601 0,2%Triton) for 30 min, left overnight with primary antibodies in PBT at 4°C, washed  
602 2 h in PBT, left with secondary antibodies in PBT for 2 hrs at room temperature,  
603 washed 1 h in PBT and mounted in Citifluor (Eikenes et al., 2015; Matias et al.,  
604 2015).

605 GSC were identified with the fusome staining (round or linking the CB) and counted.  
606 Stem-cysts (more than 2 cells anchored to the niche and linked by a fusome) and  
607 polyploid GSC (higher DNA and larger fusome than control) were counted. Stacks  
608 were acquired every 0.7 µm.

609

#### 610 **Live imaging and image analysis**

611 Live imaging was performed on pupae aged for 16 to 22h APF at 20-25°C (Gho et  
612 al., 1999). Pupae were stucked on a glass slide with a double-sided tape, and the  
613 brown pupal case was removed over the head and dorsal thorax using  
614 microdissection forceps. Pillars made of 4 to 5 glass coverslips were positioned at  
615 the anterior and posterior side of the pupae, respectively. A glass coverslip covered  
616 with a thin film of Voltalef 10S oil is then placed on top of the pillars such that a  
617 meniscus is formed between the dorsal thorax of the pupae and the glass coverslip.  
618 Images were acquired with a confocal microscope Leica SP5, SP8 or SPE equipped  
619 with a 63X N.A. 1.4. and controlled by LAS AF software. Confocal sections were  
620 taken every 0.5 µm unless otherwise specified. All images were processed and  
621 assembled using ImageJ/FIJI software and Photoshop CS4.

622

#### 623 **Fluorescence recovery after photobleaching**

624 FRAP experiments were performed in pupae expressing MyoIIIRFP with ATPαGFP  
625 and neur-GAP43IR. Regions of interest corresponding to one of the two ATPα::GFP  
626 finger-like protrusions pointing to the midbody were bleached (488 nm at 100% laser,  
627 1 iteration of 100 ms) using a LSM Leica SP8 equipped with a 63X N.A. 1.4 PlanApo  
628 objective. Confocal stacks were acquired every 2 min and 30s after photobleaching.

629

### 630 **KAEDE photoconversion**

631 Photoconversion assays were performed in pupae expressing the green to red  
632 photoconvertible probe KAEDE. KAEDE was photoconverted (405 nm laser at 0,5 to  
633 2% power, point bleach, 1 to 2 iterations of 300 ms each) using a LSM Leica SP8  
634 equipped with a 63X N.A. 1.4 PlanApo objective. Confocal stacks were acquired  
635 every 2 min after photoconversion and imaged at 22-25°C.

636

### 637 **Quantification and statistical analysis**

#### 638 **Midbody tracking**

639 The apico-basal position of the midbody was calculated measuring the distance  
640 between the middle of the new Adherens junction and the midbody (both labeled  
641 with MyoII::RFP) at each time. The x, y, z coordinates of AJ and the midbody were  
642 manually tracked to record positions at each time, and then were used to calculate  
643 the distance using the Pythagorean Theorem. The midbody apico-basal tracking  
644 movement was calculated using the equation  $y = -ax + b$ , where a corresponds to the  
645 midbody velocity toward the basal pole.

646

#### 647 **Signal recovery upon photobleaching**

648 For each FRAP experiment, three measures were performed, the photobleached  
649 junction, the control junction (the finger-like protrusion opposite to the FRAPed  
650 finger-like protrusion) and the background.

651 Data were normalized using EasyFRAP-web software with the "Full scale" method.  
652 Signal recoveries were approximated with the equation  $y = y_{max} (1 - e^{-kx})$  with the  
653 half-life  $t_{1/2} = \ln(2) / k$ .

654

#### 655 **Statistical tests**

656 All information concerning the statistical tests are provided in the main text and in the  
657 figure legends, including the number of samples analyzed in each experiment.  
658 Prism 8 software or R 4.2.1 were used to perform the analyses.  
659 Line plots use the following standards: thick lines indicate the means. Bar plots  
660 represent mean and errors bars represent the SD.

661 Shapiro-Wilk normality test was used to confirm the normality of the data and the F-  
662 test to verify the equality of SD. The statistical differences of Gaussian data sets  
663 were analyzed using the Student unpaired two-tailed t test.

664 For the analysis of the midbody displacement, we performed an ANCOVA to test the  
665 effect of the interaction between time (between 5 and 120 min) and the « condition »  
666 parameter (SOP vs EC). For the midbody displacement and FRAP, the colored  
667 areas show standard deviation (SD).

668 Time to cytoplasmic isolation was modeled via logistic regression, using the GLM  
669 function in R, with a binomial error distribution and a logistic link function. We began  
670 with a fully parameterized model in which cytoplasmic isolation varied as a function  
671 of time, condition and the interaction between time and condition (i.e. both the slopes  
672 and intercepts of the model describing temporal effects differed among condition  
673 groups). Statistical significance of each model term was evaluated via analysis of  
674 deviance, with forward model selection of terms and goodness-of-fit assessed  
675 against a Chi-squared distribution. Additionally, we ran two additional nested  
676 models: one excluding the interaction term (i.e. a common model slope with  
677 differences amongst condition groups in their intercept terms; equivalent to  
678 differences in the means amongst groups), and a second in which cytoplasmic  
679 isolation state varied only as a function of time (i.e. no effective differences amongst  
680 condition groups). We compared overall fit for each model using Akaike's  
681 information criterion (AIC), selecting the parsimony model as the one with the lowest  
682 AIC score. Results of analysis of deviance and model comparisons corroborated  
683 each other, and so the parsimony model was used to predict the mean percentage of  
684 cells demonstrating cytoplasmic isolation, as well as standard errors (SE) of the  
685 estimates, and to visualize differences among groups. In some lines, the interaction  
686 between time and treatment was not significant, however the interaction between  
687 `sca>` and `pnr>` was slightly significant (Table S1). These results were corroborated  
688 by model comparison via AIC, with the selection process favoring models including  
689 only time and treatment effects, i.e. although proportions of cells in cytoplasmic  
690 isolation differed among conditions at a given time point, the rate of relative increase  
691 over time did not differ among groups. This lack of significant time-treatment  
692 interaction facilitated the comparison of treatment effect size. To do so, we used  
693 model results to estimate the time at which 50% of the pIIa/pIIb cell indicated  
694 cytoplasmic isolation (herein termed  $t_{1/2}$ ). Each  $t_{1/2}$  were estimated using the two

695 models (sca> and sca>shrubRNAi) and (pnr>, pnr>+ ShrubGFP/+, pnr>+ Cora  
696 RNAi, pnr>Cora RNAi+ ShrubGFP/+). Statistical significance were represented as  
697 follow: p-value>0.05 ns (not significant); p-value≤0.05\*; p-value≤0.01\*\* and p-  
698 value≤0.001\*\*\*

699

700

701 **Figure Legends**

702

703 **Fig. 1. Midbody assembly and basal displacement throughout epithelial cell**  
704 **cytokinesis**

705 (A) Schematic representation of the *Drosophila* pupal notum composed of epidermal  
706 cells (white) and sensory organ precursors (SOP, grey). Adherens junctions (AJ) and  
707 septate junctions (SJ) were represented in magenta and green respectively. (A') EC  
708 daughter cells cytoplasmic isolation happens after 5 hours after anaphase onset of  
709 their mother. In the meantime, SOP undergo four rounds of asymmetric cell division.  
710 2h and 2h20 refers to the approximative time at which the respective daughter cells  
711 start to divide. At each division, fate identity relies on differential activation of Notch  
712 (Notch is activated in the cells depicted in blue).

713 (B) Time-lapse of SOP cells (n=12) expressing MyoIIIRFP (magenta), ATP $\alpha$ GFP  
714 (green) and Histone 2B IR (H2BIR) to identify the SOP (blue). B' correspond to the  
715 orthogonal views along the white dashed lines depicted at t=10 min on panel B.  
716 White arrows point to the midbody. AJ, adherens junction; SJ, septate junction; Ap:  
717 Apical; Ba: Basal.

718 (C) Localization of E-Cad (cyan) and Cora (green) at the pIIa-pIIb cell stage  
719 identified using H2BIR (white). Higher magnifications in (C') correspond to the ROI in  
720 the white dotted line square depicted in (C) and white arrows show the finger-like  
721 protrusions. (n>3, 3 nota per condition). Right: Schematic representation of the SOP  
722 with the finger like protrusions in green as in (C').

723 (D) Schematic representation of the midbody basal displacement in EC and SOP  
724 corresponding to t115 (1A' and 1B'). MB: Midbody

725 (E) Plot of the quantification of the apical to basal midbody displacement over time  
726 relative to AJs in EC (black, n=40) and SOP (blue, n=30) dividing cells. ANCOVA, p-  
727 value < 2.2.10<sup>-16</sup>\*\*\*. Solid lines represent simple linear fit.

728 Time is in minute with t= 0 corresponding to anaphase onset (B-B', E). Scale bars  
729 represent 5  $\mu$ m (B-C) and 1  $\mu$ m (C'). Red and blue dots mark the pIIb and pIIa  
730 respectively (B-C).

731

732 **Fig. S1: Midbody assembly and basal displacement throughout EC**  
733 **cytokinesis**

734 (A) Time-lapse of EC dividing cells (n=20) expressing MyoIIIRFP (magenta),  
735 ATP $\alpha$ GFP (green). A' correspond to the orthogonal views along the white dashed  
736 lines depicted at t=10 min on panels A. White arrows point to the midbody. AJ,  
737 adherens junction; SJ, septate junction; Ap: Apical; Ba: Basal. Time is in minutes  
738 with t=0 corresponding to anaphase onset and scale bars represents 5  $\mu$ m.

739

740

## 741 **Fig. 2. Kinetics of SJ assembly in SOP and EC**

742 (A) Time lapse of SOP (n=5) dividing cells expressing MyoIIIRFP and nlsRFP  
743 (magenta) and H2BIR (white) adjacent to cells expressing MyoIIIRFP (magenta) and  
744 ATP $\alpha$ GFP (green and grey on upper and bottom panels, respectively). Distances in  
745  $\mu$ m represent the position relative to the AJ plane determined by apical MyoII signal.  
746 White dashed line delineates the clone border at t0. White arrows point to the  
747 midbody. Dashed white ring encircles the midbody at t110 and t120. The white  
748 square at t120 represents a higher magnification of the midbody located below a  
749 nucleus expressing nlsRFP (scale bar represents 1  $\mu$ m).

750 (B) Time lapse of dividing SOP (n=2) expressing MyoIIIRFP (magenta), H2BIR  
751 (white) and ATP $\alpha$ GFP (green) close to cells expressing MyoIIIRFP (magenta) and  
752 nlsRFP (magenta). Dashed white ring encircles the midbody at t120. Distances in  
753  $\mu$ m represent the position relative to the AJ plane determined by apical MyoII signal.

754 (C) Time lapse of SOP dividing cell expressing MyoIIIRFP (magenta), ATP $\alpha$ GFP  
755 (green and grey on upper and second panels, respectively) and the plasma  
756 membrane marker GAP43IR (blue), and FRAP of ATP $\alpha$ GFP. Yellow dotted line  
757 square inset indicates the photobleached region of interest. The white dotted line  
758 rectangle at t=0 delineate the ROI shown in the right panels (t=10-40 min) at the  
759 level of SJ and MB to monitor the recovery of ATP $\alpha$ GFP signal over time.  
760 Photobleaching was done 20 min after the anaphase onset with t=0 corresponding to  
761 the time of photobleaching.

762 (D) Plot of the quantification of fluorescence recovery of ATP $\alpha$ GFP signal after  
763 photobleaching over time in EC (n=20, black) and SOP (n=13, blue) in the SJ plane  
764 located 1  $\mu$ m below AJ. Solid white lines represent a simple exponential fit.

765 AJ: Adherens junctions, SJ: Septate junctions, MB: Midbody. In A, B, and C, SOPs  
766 and daughters were identified using H2BIR in A and B (grey) or GAP43IR in C  
767 (blue). Red and blue dots mark the pIIb and pIIa respectively (A-C). Time is in

768 minutes with  $t_0$  corresponding to the onset of SOP anaphase, except in (C, D) where  
769  $t_0$  corresponds to the time of photobleaching. Scale bars represent 5  $\mu\text{m}$  (A-B) and 3  
770  $\mu\text{m}$  (C).

771

772

773 **Fig. S2: Evolution of SJ-positive finger-like protrusions and midbody contacts**  
774 **throughout EC cytokinesis**

775 (A) Time lapse of EC (A,  $n=13$ ) dividing cells expressing MyoII-RFP (magenta),  
776 nlsRFP (magenta) close to cells expressing MyoII-RFP (magenta) and ATP $\alpha$ GFP  
777 (green, grey bottom panels). White dashed lines delineate the clone border at  $t_0$ .  
778 White arrows point to the midbody. AJ, adherens junction; SJ, septate junction. Time  
779 is in minutes with  $t_0$  corresponding to the onset of anaphase. Scale bar represents 5  
780  $\mu\text{m}$ .

781

782 **Fig. 3. cytoplasmic isolation of pll $a$ -pll $b$  and midbody release are temporally**  
783 **controlled**

784 (A-B) Time lapse of SOP dividing cell expressing KAEDE under *pannier* driver.  
785 Green to Red (magenta) photoconversion was performed (yellow lightning at  $t=0$ ) in  
786 the pll $b$  cell at 61 min (A) or 63 min (B) after the onset of anaphase. A' and B'  
787 correspond to the orthogonal views along the white dashed lines depicted at  $t=-1$  min  
788 on panels A and B, respectively. Ap: Apical, Ba: Basal. Time is in min where  $t=0$   
789 corresponds to the time of photoconversion.

790 (C) Plot representing the proportion of pll $a$ -pll $b$  cells to have cytoplasmic isolation  
791 over time after anaphase onset in control (*pnr*>). Cytoplasmic isolation was  
792 assessed based on the ability of photo-converted KAEDE in pll $a$ /pll $b$  cell to diffuse in  
793 the pll $b$ /pll $a$  cell at different time point after the onset of anaphase. The dashed line  
794 represents mean values, predicted from a generalized linear model (GLM). SE of the  
795 estimates are represented in grey shading.  $n=62$ , 24 pupae.

796 (D) Time lapse of SOP dividing cell expressing MyoII-GFP (Green) and GAP43-IR  
797 (Magenta). White arrows point to the midbody. Distances in  $\mu\text{m}$  represent the  
798 position relative to the AJ plane determined by apical MyoII signal. (D') corresponds  
799 to the orthogonal view depicted in (D,  $t=110$ ). (D'') scheme representing the  
800 displacement of the midbody over the pll $a$  membrane at the indicated time as in (D)

801 and adapted from (Houssin et al., 2021). The red and blue cells correspond to the  
802 pIIb and pIIb respectively. Ap: Apical; Ba: Basal.

803 (E) Timeline of events during SOP cytokinesis

804 AJ: Adherens junctions, MB: Midbody. Red and blue dots mark the pIIb and pIIa  
805 respectively (A, B, D). Time is in minutes with t<sub>0</sub> corresponding to the onset of  
806 anaphase (D) except in A and B where t<sub>0</sub> corresponds to the time of  
807 photoconversion. Scale bars represent 5 μm (A-B,D-D').

808

809 **Fig. S3: Maturation of the midbody and timing of cytoplasmic isolation**

810 (A) Schematic representation of KAEDE photoconversion in SOP cells. The two  
811 daughter cells (pIIa and pIIb) are both expressing KAEDE (Green). After  
812 photoconversion in pIIa cell, Green KAEDE is photoconverted into Red KAEDE  
813 (Magenta). 2 min to until its equilibrium at 8 min after photoconversion, Red KAEDE  
814 diffuses in the pIIb cell (No cytoplasmic isolation) or do not diffuse into pIIb  
815 (Cytoplasmic isolation). adapted from (Houssin et al., 2021)

816 (B) Frequency of pIIa-pIIb control cells *pnr*> (black) and *sca*> (grey) photo-converted  
817 at different time after anaphase onset.

818 (C) Plot representing the proportion of pIIa-pIIb cells to have cytoplasmic isolation  
819 over time after anaphase onset in control *pnr*> (*pnr*>, dashed line, n=62, 24 pupae)  
820 and control *sca*> (*sca*>, solid line, n=30, 11 pupae). Cytoplasmic isolation was  
821 assessed based on the ability of photo-converted KAEDE in pIIa/pIIb cell to diffuse in  
822 the pIIb/pIIa cell at different time point after the onset of anaphase. Lines represent  
823 mean values, predicted from a GLM with the interaction between time and  
824 conditions; SE of the estimates are represented in grey shading.

825 (D) Frequency of pIIa-pIIb control cells (*sca*>) photo-converted at different time after  
826 anaphase onset.

827 (E) Time lapse of SOP dividing cells expressing MyoIIIRFP (magenta), MyoIIGFP  
828 (green) and GAP43IR (grey). White arrows point to the midbody. (E') Higher  
829 magnification of the white dashed square depicted at t<sub>0</sub> in (E) shows the midbody.

830 (F) Time lapse of SOP dividing cells expressing MyoIIIRFP (magenta), PavGFP  
831 (green) and GAP43IR (grey). White arrows point to the midbody. (F') Higher  
832 magnification of the white dashed square depicted at t<sub>0</sub> in (F) shows the midbody.

833 Time is in minutes. Blue dots mark the pIIa (E, F). Scale bars represent 5 μm (E-F')  
834 and 1 μm (E', F').

835

836

837 **Fig. 4. Recruitment and function of Shrub in SOP daughter cells**

838 (A-A') Time lapse of SOP dividing cells expressing MyoIIIRFP (magenta), ShrubGFP  
839 (green) and GAP43IR (grey). (A') Higher magnification of the white dashed line inset  
840 depicted in (A) at t10 showing the recruitment of ShrubGFP (green) at the midbody  
841 (magenta) over time. (A'') Schematic representation depicting ShrubGFP recruitment  
842 at the presumptive finger like protrusions (between 40 and 60 min) and (A''') at the  
843 midbody (magenta square) (between 70 and 120 min) corresponding to (A').

844 (B) Time lapse of SOP dividing cell expressing MyoIIImcherry (magenta) adjacent to  
845 epidermal cell expressing MyoIIImCherry (magenta) together with ShrubGFP  
846 expressed under *Ay Gal4* driver (green). White line delineates the border of clones of  
847 cells expressing ShrubGFP at t0. The higher magnifications at the bottom right (MB  
848 level, t10-72) correspond to the ROI in the white dotted line square of the  
849 corresponding panel (scale bar represents 1  $\mu$ m). (B') Representation of the SOP at  
850 t36 (B) surrounded by one EC positive for ShrubGFP (light green) and showing the  
851 ShrubGFP puncta (dark green) at the tip of the finger-like protrusion pointing toward  
852 the midbody (magenta square).

853 (C) Time lapse of dividing SOP expressing MyoIIImcherry (magenta) together with  
854 ShrubGFP expressed under *Ay Gal4* driver (Green) close to cells expressing  
855 MyoIIImcherry (magenta) but not ShrubGFP. White dashed line delineates the clone  
856 border at t=0. The higher magnifications at the bottom right (MB level, t10-90)  
857 correspond to the ROI in the white dotted line square of the corresponding panel  
858 (scale bar represents 1  $\mu$ m). (C') Representation of the ShrubGFP positive SOP  
859 (light green) at t60 (C) surrounded by ECs negative for ShrubGFP and showing the  
860 ShrubGFP punctae (dark green) recruitment at the midbody (magenta square).

861 (D) Localization of KAEDE (green), Kune Kune (magenta) and Crumbs (grey) in *nota*  
862 expressing Shrub RNAi and KAEDE. The white dashed lines separate control from  
863 Shrub RNAi (KAEDE expressing cells). Ap: apical, Ba: basal.

864 (E) Plot representing the proportion of pIIa-pIIb cells to have cytoplasmic isolation  
865 over time after anaphase onset. Cytoplasmic isolation was assessed based on the  
866 ability of photo-converted KAEDE in pIIa/pIIb cell to diffuse in the pIIb/pIIa cell at  
867 different time point after the onset of anaphase in control (*sca*>, solid line, n=30, 11  
868 pupae) and ShrubRNAi (*sca*> ShrubRNAi, dashed line, n=30, 14 pupae). Lines

869 represent mean values, predicted from a GLM of t1/2 values for *sca>* centered to 0;  
870 SE of the estimates are represented in grey shading. p-value=0,003, \*\*)

871

872 **Fig. S4: Recruitment of Shrub at the midbody and function of Shrub in**  
873 **cytoplasmic isolation**

874 (A) Time lapse of EC dividing cell expressing MyoIImcherry adjacent to cells  
875 expressing MyoIImcherry (magenta) together with ShrubGFP expressed under *Ay*  
876 *Gal4* driver (green). White line delineates the border of clones of cells expressing  
877 ShrubGFP at t0. The higher magnifications at the bottom right (MB level, t10-36)  
878 correspond to the ROI in the white dotted line square of the corresponding panel  
879 (scale bar represents 1  $\mu$ m). (A') Representation of the EC at t36 (A) surrounded by  
880 EC positive for ShrubGFP (light green) and showing the ShrubGFP punctae (dark  
881 green) recruitment at the tip of the finger-like protrusion pointing toward the midbody  
882 (magenta square).

883 (B) Time lapse of dividing EC expressing MyoIImcherry (magenta) together with  
884 ShrubGFP under the *Ay Gal4* driver (Green) close to cells expressing MyoIIIRFP  
885 (magenta) but not ShrubGFP. White dashed line delineates the clone border at t=0.  
886 The higher magnifications at the bottom right (MB level, t12-90) correspond to the  
887 ROI in the white dotted line square of the corresponding panel (scale bar represents  
888 1  $\mu$ m). (B') Representation of the ShrubGFP positive EC (light green) at t60 (B)  
889 surrounded by ECs negative for ShrubGFP and showing the ShrubGFP puncta (dark  
890 green) recruitment at the midbody (magenta square).

891 (C) Localization of KAEDE (green) and HRS (magenta) in nota expressing Shrub  
892 RNAi and KAEDE. The white dashed lines separate control from Shrub RNAi  
893 (KAEDE expressing cells).

894 (D) Localization of KAEDE (green) and NrXIV (magenta) in nota expressing Shrub  
895 RNAi and KAEDE. The white dashed lines separate control from Shrub RNAi  
896 (KAEDE expressing cells).

897 (E) Localization of KAEDE (green) and Sinus (magenta) in nota expressing Shrub  
898 RNAi and KAEDE. The white dashed lines separate control from Shrub RNAi  
899 (KAEDE expressing cells).

900 (F) Higher magnification of a SOP midbody (magenta) showing CHMP2BGFP  
901 recruitment (green).

902 AJ, adherens junction; MB, Midbody. Time is in minutes with t0 corresponding to  
903 anaphase onset (A-B'). Scale bars represent 5  $\mu\text{m}$  (A, B, C-E) and 1  $\mu\text{m}$  (F).

904

905 **Fig. 5. ShrubGFP is a mutant allele that impacts the timing of cytoplasmic**  
906 **isolation**

907 (A) Plot representing the proportion of pIIa-pIIb cells to have cytoplasmic isolation  
908 over time after anaphase onset. Cytoplasmic isolation was assessed based on the  
909 ability of photo-converted KAEDE in pIIa/pIIb cell to diffuse in the pIIb/pIIa cell at  
910 different time point after the onset of anaphase in control (*pnr* >, dashed line, n=62,  
911 24 pupae) and ShrubGFP/+ (*pnr* >+ ShrubGFP/+ ,dotted line, n=52, 12 pupae).

912 Lines represent mean values, predicted from a GLM of t1/2 values for *pnr*> centered  
913 to 0; SE of the estimates are represented in grey shading (p-value= $1,68 \cdot 10^{-6}$ , \*\*\*).

914 Time is in minutes.

915

916 **Fig. S5:**

917 (A) Z-projection of confocal images obtained on control (left) or ShrubGFP/+ ovaries  
918 (green, middle and right) stained for  $\alpha$ -Spectrin (magenta) to visualize the fusome  
919 linking the germline stem cell (GSC) to its progeny. In control, the GSC is only linked  
920 to its daughter cystoblast (CB). In ShrubGFP/+ ovaries, GSC are either as in control  
921 (middle) or linked to several progeny and form stem cysts (right). Scale bars  
922 represent 5  $\mu\text{m}$ .

923 (B) Higher magnification of a SOP midbody (magenta) showing CHMP2BGFP  
924 recruitment (green). Scale bars represent 1  $\mu\text{m}$ .

925

926

927 **Fig. 6. Interplay between Shrub and SJ components in the control of**  
928 **cytoplasmic isolation**

929 (A) Localization of Cora (magenta) upon silencing of Cora (A). The white dashed  
930 lines separate wild type from KAEDE expressing cells, which correspond to the area  
931 of Cora depletion.

932 (B) Plot representing the proportion of pIIa-pIIb cells to have cytoplasmic isolation  
933 over time after anaphase onset. Cytoplasmic isolation was assessed based on the  
934 ability of photo-converted KAEDE in pIIa/pIIb cell to diffuse in the pIIb/pIIa cell at

935 different time point after the onset of anaphase in control (*pnr*>, dashed line, n=62,  
936 24 pupae), Cora RNAi (*pnr*>CoraRNAi, dotdashed line, n=32, 16 pupae),  
937 ShrubGFP/+ (*pnr*>+ ShrubGFP/+, dotted line, n=52, 12 pupae) and Cora RNAi +  
938 ShrubGFP/+ (*pnr*>CoraRNAi+ShrubGFP/+ solid line, n=30, 6 pupae). Lines  
939 represent mean values, predicted from a GLM of t1/2 values for *pnr*> centered to 0;  
940 SE of the estimates are represented in grey shading. (*pnr*> vs *pnr*>CoraRNAi, p-  
941 value=0,029,\*; *pnr*> vs Cora RNAi + ShrubGFP/+, p-value=0.425, ns; Cora RNAi +  
942 ShrubGFP/+ vs *pnr*>+ ShrubGFP/+, p-value=4,52.10<sup>-7</sup>,\*\*\*; *pnr*>CoraRNAi vs Cora  
943 RNAi + ShrubGFP/+, p-value=0.075,ns).

944 (C) Time lapse of SOP dividing cell depleted of Cora expressing MyoII GFP (Green)  
945 and GAP43IR (Magenta). White arrows point to the midbody. Distances in  $\mu\text{m}$   
946 represent the position relative to the AJ plane determined by apical MyoII signal.

947 (D) Plot representing the time after anaphase onset (min) when the midbody is  
948 released from the new interface between pll<sub>b</sub> and pll<sub>a</sub> in control (white, n=12) and  
949 Cora depleted cells (light grey, n=8). Time is in min. (unpaired t-tests; p-value=0,002,  
950 \*\*)

951 (E) Plot representing the time after anaphase onset (min) when the midbody is  
952 disappearing from the SOP in control (white, n=13) and Cora depleted cells (light  
953 grey, n=7). Time is in min. (unpaired t-tests; p-value=0.0004, \*\*\*)

954 (F) Plot of the time of the onset of pll<sub>a</sub> and pll<sub>b</sub> anaphase after the onset of SOP  
955 anaphase in control (black, n=13) and Cora depleted (grey, n=8) cells. Time is in  
956 min. (unpaired t-tests; p-value=0.000045 and p-value=0,00081,\*\*\* for pll<sub>b</sub> and pll<sub>a</sub>  
957 respectively)

958 (G) Time lapse of SOPs expressing MyoII RFP (magenta) and ShrubGFP (green)  
959 depleted from Cora. (G') Higher magnifications of the white dotted square inset  
960 depicted in (C) at t10 showing ShrubGFP (green) recruitment to the midbody  
961 (magenta) (n= 2/6).

962 (H) Scheme depicting Shrub recruitment (Green) in the finger-like protrusions and at  
963 the level of the midbody (magenta rectangle) during cytokinesis in SOP control and  
964 depleted with Cora RNAi.

965 (I) Scheme proposing a model representing Shrub functions during epithelial  
966 cytokinesis. Shrub exerts a cell autonomous function in the control of the separation  
967 of the pll<sub>a</sub>-pll<sub>b</sub> cytoplasm. Shrub (green spiral) is recruited at the level of the  
968 midbody (magenta rectangle). Shrub exerts a cell non-autonomous function in the

969 remodeling of the SJs within the finger-like protrusions. This activity is linked to SJ  
970 trafficking via endosomes.

971 Time is in minutes with t0 corresponding to the onset of anaphase (C-E, G-G'). Red  
972 and blue dots mark the p11b and p11a respectively (C, G). Scale bars represent 5  $\mu$ m  
973 (A, C, G) and 1  $\mu$ m (G').

974

975

976

977

978

## 979 **References**

980 **Agromayor, M. and Martin-Serrano, J.** (2013). Knowing when to cut and run:  
981 mechanisms that control cytokinetic abscission. *Trends Cell Biol.* **23**, 433–  
982 441.

983 **Ando, R., Hama, H., Yamamoto-Hino, M., Mizuno, H. and Miyawaki, A.** (2002).  
984 An optical marker based on the UV-induced green-to-red photoconversion of  
985 a fluorescent protein. *Proceedings of the National Academy of Sciences* **99**,  
986 12651–12656.

987 **Audibert, A.** (2005). Cell cycle diversity involves differential regulation of Cyclin E  
988 activity in the Drosophila bristle cell lineage. *Development* **132**, 2287–2297.

989 **Babst, M., Katzmann, D. J., Estepa-Sabal, E. J., Meerloo, T. and Emr, S. D.**  
990 (2002). Escrt-III: an endosome-associated heterooligomeric protein complex  
991 required for mvb sorting. *Dev Cell* **3**, 271–282.

992 **Banerjee, S., Sousa, A. D. and Bhat, M. A.** (2006). Organization and function of  
993 septate junctions: an evolutionary perspective. *Cell Biochem. Biophys.* **46**,  
994 65–77.

995 **Bellec, K., Gicquel, I. and Le Borgne, R.** (2018). Stratum recruits Rab8 at Golgi  
996 exit sites to regulate the basolateral sorting of Notch and Sanpodo.  
997 *Development* **145**, dev163469.

998 **Calleja, M., Moreno, E., Pelaz, S. and Morata, G.** (1996). Visualization of gene  
999 expression in living adult Drosophila. *Science* **274**, 252–255.

1000 **Chaigne, A., Labouesse, C., White, I. J., Agnew, M., Hannezo, E., Chalut, K. J.**  
1001 **and Paluch, E. K.** (2020). Abscission Couples Cell Division to Embryonic  
1002 Stem Cell Fate. *Dev Cell* **55**, 195-208.e5.

1003 **Couturier, L., Vodovar, N. and Schweisguth, F.** (2012). Endocytosis by Numb  
1004 breaks Notch symmetry at cytokinesis. *Nat Cell Biol* **14**, 131–139.

- 1005 **Couturier, L., Trylinski, M., Mazouni, K., Darnet, L. and Schweisguth, F.** (2014).  
1006 A fluorescent tagging approach in *Drosophila* reveals late endosomal  
1007 trafficking of Notch and Sanpodo. *J Cell Biol* **207**, 351–363.
- 1008 **Crowell, E. F., Gaffuri, A.-L., Gayraud-Morel, B., Tajbakhsh, S. and Echard, A.**  
1009 (2014). Engulfment of the midbody remnant after cytokinesis in mammalian  
1010 cells. *J Cell Sci* **127**, 3840–3851.
- 1011 **Daniel, E., Daudé, M., Kolotuev, I., Charish, K., Auld, V. and Le Borgne, R.**  
1012 (2018). Coordination of Septate Junctions Assembly and Completion of  
1013 Cytokinesis in Proliferative Epithelial Tissues. *Curr. Biol.* **28**, 1380-1391.e4.
- 1014 **Dong, B., Hannezo, E. and Hayashi, S.** (2014). Balance between Apical Membrane  
1015 Growth and Luminal Matrix Resistance Determines Epithelial Tubule Shape.  
1016 *Cell Reports* **7**, 941–950.
- 1017 **Dubreuil, V., Marzesco, A.-M., Corbeil, D., Huttner, W. B. and Wilsch-**  
1018 **Bräuninger, M.** (2007). Midbody and primary cilium of neural progenitors  
1019 release extracellular membrane particles enriched in the stem cell marker  
1020 prominin-1. *J. Cell Biol.* **176**, 483–495.
- 1021 **Dukes, J. D., Fish, L., Richardson, J. D., Blaikley, E., Burns, S., Caunt, C. J.,**  
1022 **Chalmers, A. D. and Whitley, P.** (2011). Functional ESCRT machinery is  
1023 required for constitutive recycling of claudin-1 and maintenance of polarity in  
1024 vertebrate epithelial cells. *Mol Biol Cell* **22**, 3192–3205.
- 1025 **Eikenes, Å. H., Malerød, L., Christensen, A. L., Steen, C. B., Mathieu, J., Nezis,**  
1026 **I. P., Liestøl, K., Huynh, J.-R., Stenmark, H. and Haglund, K.** (2015). ALIX  
1027 and ESCRT-III Coordinately Control Cytokinetic Abscission during Germline  
1028 Stem Cell Division In Vivo. *PLoS Genet* **11**, e1004904.
- 1029 **Esmangart de Bournonville, T. and Le Borgne, R.** (2020). Interplay between  
1030 Anakonda, Gliotactin, and M6 for Tricellular Junction Assembly and Anchoring  
1031 of Septate Junctions in *Drosophila* Epithelium. *Curr Biol* **30**, 4245-4253.e4.
- 1032 **Ettinger, A. W., Wilsch-Bräuninger, M., Marzesco, A.-M., Bickle, M., Lohmann,**  
1033 **A., Maliga, Z., Karbanová, J., Corbeil, D., Hyman, A. A. and Huttner, W. B.**  
1034 (2011). Proliferating versus differentiating stem and cancer cells exhibit  
1035 distinct midbody-release behaviour. *Nat Commun* **2**, 503.
- 1036 **Faivre-Sarrailh, C.** (2020). Molecular organization and function of vertebrate  
1037 septate-like junctions. *Biochimica et Biophysica Acta (BBA) - Biomembranes*  
1038 **1862**, 183211.
- 1039 **Fededa, J. P. and Gerlich, D. W.** (2012). Molecular control of animal cell  
1040 cytokinesis. *Nat. Cell Biol.* **14**, 440–447.
- 1041 **Fichelson, P. and Gho, M.** (2003). The glial cell undergoes apoptosis in the  
1042 microchaete lineage of *Drosophila*. *Development* **130**, 123–133.

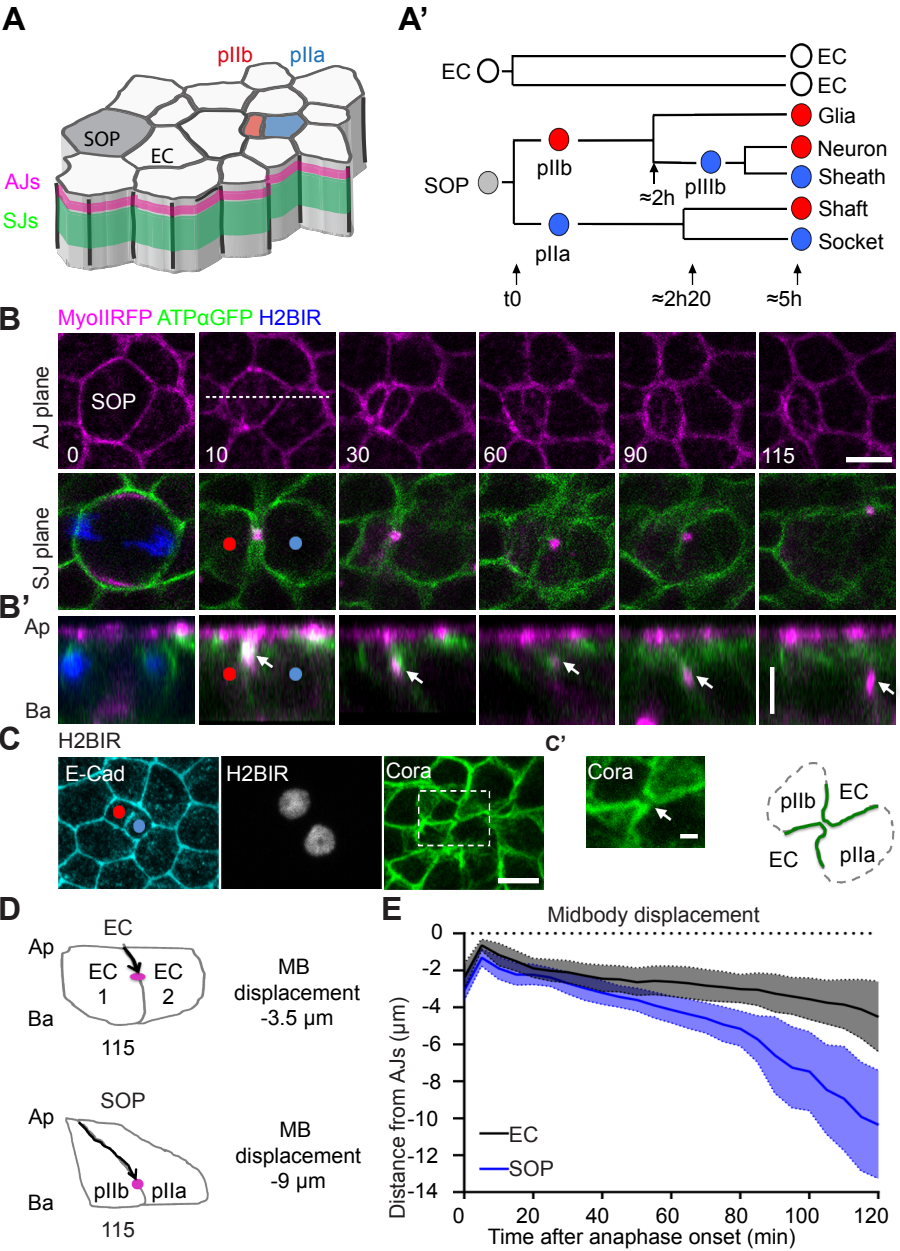
- 1043 **Firmino, J., Rocancourt, D., Saadaoui, M., Moreau, C. and Gros, J.** (2016). Cell  
1044 Division Drives Epithelial Cell Rearrangements during Gastrulation in Chick.  
1045 *Dev. Cell* **36**, 249–261.
- 1046 **Founounou, N., Loyer, N. and Le Borgne, R.** (2013). Septins regulate the  
1047 contractility of the actomyosin ring to enable adherens junction remodeling  
1048 during cytokinesis of epithelial cells. *Dev. Cell* **24**, 242–255.
- 1049 **Genova, J. L. and Fehon, R. G.** (2003). Neuroglian, Gliotactin, and the Na<sup>+</sup>/K<sup>+</sup>  
1050 ATPase are essential for septate junction function in *Drosophila*. *Journal of*  
1051 *Cell Biology* **161**, 979–989.
- 1052 **Gho, M., Lecourtois, M., Géraud, G., Posakony, J. W. and Schweisguth, F.**  
1053 (1996). Subcellular localization of Suppressor of Hairless in *Drosophila* sense  
1054 organ cells during Notch signalling. *Development* **122**, 1673–1682.
- 1055 **Gho, M., Bellaïche, Y. and Schweisguth, F.** (1999). Revisiting the *Drosophila*  
1056 microchaete lineage: a novel intrinsically asymmetric cell division generates a  
1057 glial cell. *Development* **126**, 3573–3584.
- 1058 **Glotzer, M.** (2005). The molecular requirements for cytokinesis. *Science* **307**, 1735–  
1059 1739.
- 1060 **Green, R. A., Paluch, E. and Oegema, K.** (2012). Cytokinesis in animal cells. *Annu.*  
1061 *Rev. Cell Dev. Biol.* **28**, 29–58.
- 1062 **Green, R. A., Mayers, J. R., Wang, S., Lewellyn, L., Desai, A., Audhya, A. and**  
1063 **Oegema, K.** (2013). The midbody ring scaffolds the abscission machinery in  
1064 the absence of midbody microtubules. *Journal of Cell Biology* **203**, 505–520.
- 1065 **Guillot, C. and Lecuit, T.** (2013). Adhesion disengagement uncouples intrinsic and  
1066 extrinsic forces to drive cytokinesis in epithelial tissues. *Dev. Cell* **24**, 227–  
1067 241.
- 1068 **Guizetti, J., Schermelleh, L., Mäntler, J., Maar, S., Poser, I., Leonhardt, H.,**  
1069 **Müller-Reichert, T. and Gerlich, D. W.** (2011). Cortical constriction during  
1070 abscission involves helices of ESCRT-III-dependent filaments. *Science* **331**,  
1071 1616–1620.
- 1072 **Harris, T. J. C. and Tepass, U.** (2010). Adherens junctions: from molecules to  
1073 morphogenesis. *Nat. Rev. Mol. Cell Biol.* **11**, 502–514.
- 1074 **Hartenstein, V. and Posakony, J. W.** (1989). Development of adult sensilla on the  
1075 wing and notum of *Drosophila melanogaster*. *Development* **107**, 389–405.
- 1076 **Hay, B. A., Wolff, T. and Rubin, G. M.** (1994). Expression of baculovirus P35  
1077 prevents cell death in *Drosophila*. *Development* **120**, 2121–2129.
- 1078 **Herszterg, S., Leibfried, A., Bosveld, F., Martin, C. and Bellaïche, Y.** (2013).  
1079 Interplay between the dividing cell and its neighbors regulates adherens  
1080 junction formation during cytokinesis in epithelial tissue. *Dev. Cell* **24**, 256–  
1081 270.

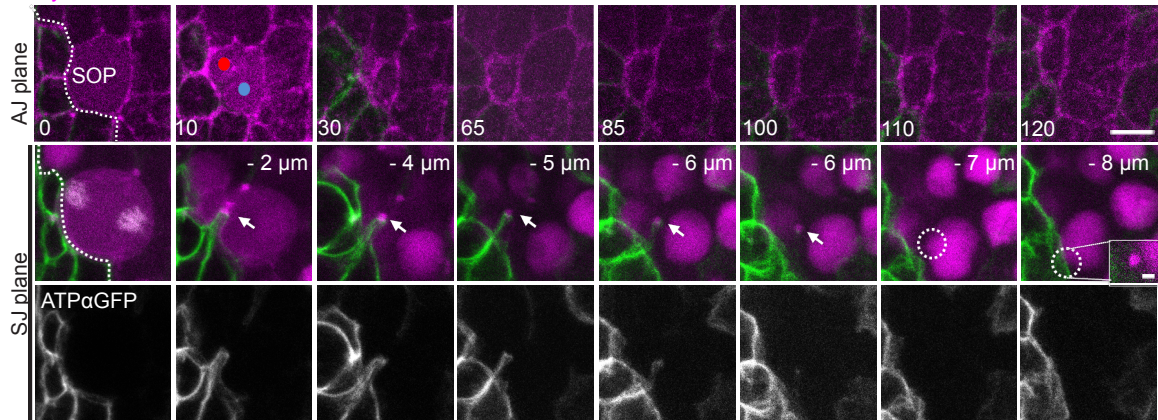
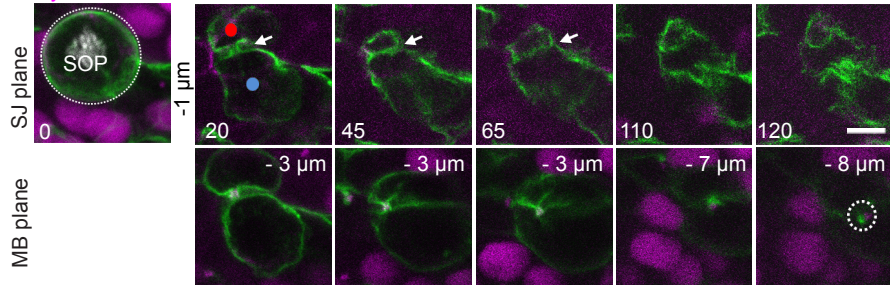
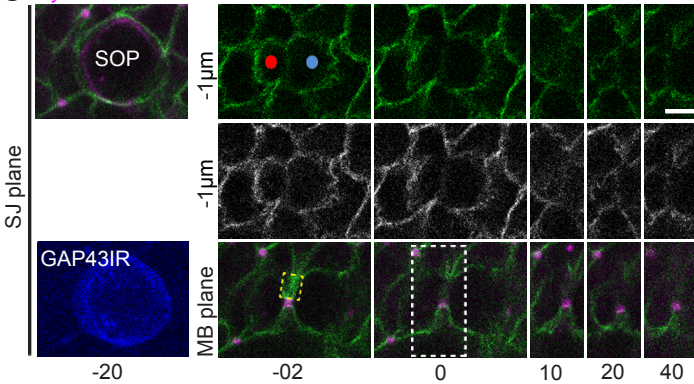
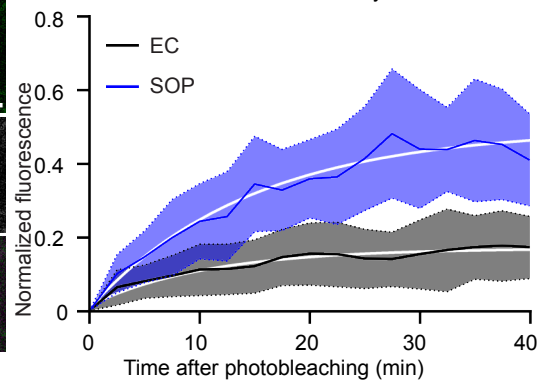
- 1082 **Higashi, T., Arnold, T. R., Stephenson, R. E., Dinshaw, K. M. and Miller, A. L.**  
1083 (2016). Maintenance of the Epithelial Barrier and Remodeling of Cell-Cell  
1084 Junctions during Cytokinesis. *Curr. Biol.* **26**, 1829–1842.
- 1085 **Houssin, E., Pinot, M., Bellec, K. and Le Borgne, R.** (2021). Par3 cooperates with  
1086 Sanpodo for the assembly of Notch clusters following asymmetric division of  
1087 *Drosophila* sensory organ precursor cells. *Elife* **10**, e66659.
- 1088 **Izumi, Y. and Furuse, M.** (2014). Molecular organization and function of invertebrate  
1089 occluding junctions. *Seminars in Cell & Developmental Biology* **36**, 186–193.
- 1090 **Jimenez, A. J., Maiuri, P., Lafaurie-Janvore, J., Divoux, S., Piel, M. and Perez, F.**  
1091 (2014). ESCRT machinery is required for plasma membrane repair. *Science*  
1092 **343**, 1247136.
- 1093 **Jinguji, Y. and Ishikawa, H.** (1992). Electron microscopic observations on the  
1094 maintenance of the tight junction during cell division in the epithelium of the  
1095 mouse small intestine. *Cell Struct. Funct.* **17**, 27–37.
- 1096 **Kaplan, J. H.** (2002). Biochemistry of Na,K-ATPase. *Annu Rev Biochem* **71**, 511–  
1097 535.
- 1098 **Kuo, T.-C., Chen, C.-T., Baron, D., Onder, T. T., Loewer, S., Almeida, S.,**  
1099 **Weismann, C. M., Xu, P., Houghton, J.-M., Gao, F.-B., et al.** (2011).  
1100 Midbody accumulation through evasion of autophagy contributes to cellular  
1101 reprogramming and tumorigenicity. *Nat Cell Biol* **13**, 1214–1223.
- 1102 **Langevin, J., Le Borgne, R., Rosenfeld, F., Gho, M., Schweisguth, F. and**  
1103 **Bellaïche, Y.** (2005). Lethal giant larvae controls the localization of notch-  
1104 signaling regulators numb, neuralized, and Sanpodo in *Drosophila* sensory-  
1105 organ precursor cells. *Curr. Biol.* **15**, 955–962.
- 1106 **Lau, K., Tao, H., Liu, H., Wen, J., Sturgeon, K., Sorfazlian, N., Lazic, S.,**  
1107 **Burrows, J. T. A., Wong, M. D., Li, D., et al.** (2015). Anisotropic stress  
1108 orients remodelling of mammalian limb bud ectoderm. *Nat. Cell Biol.* **17**, 569–  
1109 579.
- 1110 **Le Borgne, R. and Schweisguth, F.** (2003). Unequal segregation of Neuralized  
1111 biases Notch activation during asymmetric cell division. *Dev. Cell* **5**, 139–148.
- 1112 **Lengefeld, J. and Barral, Y.** (2018). Asymmetric Segregation of Aged Spindle Pole  
1113 Bodies During Cell Division: Mechanisms and Relevance Beyond Budding  
1114 Yeast? *Bioessays* **40**, e1800038.
- 1115 **Lie-Jensen, A., Ivanauskiene, K., Malerød, L., Jain, A., Tan, K. W., Laerdahl, J.**  
1116 **K., Liestøl, K., Stenmark, H. and Haglund, K.** (2019). Centralspindlin  
1117 Recruits ALIX to the Midbody during Cytokinetic Abscission in *Drosophila* via  
1118 a Mechanism Analogous to Virus Budding. *Curr Biol* **29**, 3538-3548.e7.
- 1119 **Martin, A. C., Kaschube, M. and Wieschaus, E. F.** (2009). Pulsed contractions of  
1120 an actin–myosin network drive apical constriction. *Nature* **457**, 495–499.

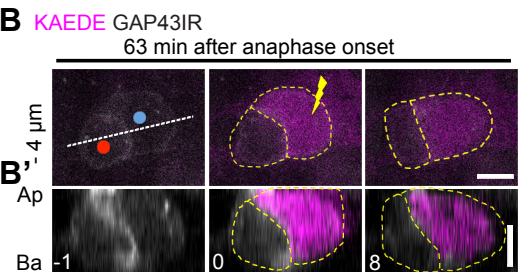
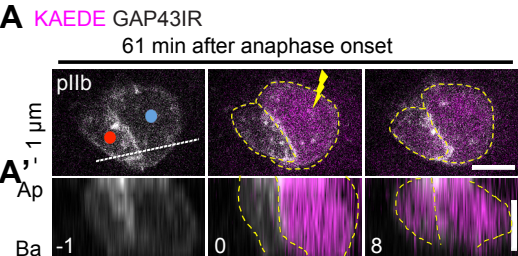
- 1121 **Mathieu, J., Cauvin, C., Moch, C., Radford, S. J., Sampaio, P., Perdigoto, C. N.,**  
1122 **Schweisguth, F., Bardin, A. J., Sunkel, C. E., McKim, K., et al.** (2013).  
1123 Aurora B and Cyclin B Have Opposite Effects on the Timing of Cytokinesis  
1124 Abscission in Drosophila Germ Cells and in Vertebrate Somatic Cells.  
1125 *Developmental Cell* **26**, 250–265.
- 1126 **Mathieu, J., Michel-Hissier, P., Boucherit, V. and Huynh, J.-R.** (2022). The  
1127 deubiquitinase USP8 targets ESCRT-III to promote incomplete cell division.  
1128 *Science* **376**, 818–823.
- 1129 **Matias, N. R., Mathieu, J. and Huynh, J.-R.** (2015). Abscission Is Regulated by the  
1130 ESCRT-III Protein Shrub in Drosophila Germline Stem Cells. *PLoS Genet* **11**,  
1131 e1004653.
- 1132 **Mlodzik, M., Baker, N. E. and Rubin, G. M.** (1990). Isolation and expression of  
1133 scabrous, a gene regulating neurogenesis in Drosophila. *Genes Dev* **4**, 1848–  
1134 1861.
- 1135 **Morais-de-Sá, E. and Sunkel, C.** (2013). Adherens junctions determine the apical  
1136 position of the midbody during follicular epithelial cell division. *EMBO Rep.* **14**,  
1137 696–703.
- 1138 **Mullins, J. and Biesele, J.** (1977). Terminal phase of cytokinesis in D-98S cells.  
1139 *Journal of Cell Biology* **73**, 672–684.
- 1140 **Nelson, K. S., Furuse, M. and Beitel, G. J.** (2010). The Drosophila Claudin Kune-  
1141 kune is required for septate junction organization and tracheal tube size  
1142 control. *Genetics* **185**, 831–839.
- 1143 **Nilton, A., Oshima, K., Zare, F., Byri, S., Nannmark, U., Nyberg, K. G., Fehon, R.**  
1144 **G. and Uv, A. E.** (2010). Crooked, Coiled and Crimped are three Ly6-like  
1145 proteins required for proper localization of septate junction components.  
1146 *Development* **137**, 2427–2437.
- 1147 **Norden, C., Mendoza, M., Dobbelaere, J., Kotwaliwale, C. V., Biggins, S. and**  
1148 **Barral, Y.** (2006). The NoCut Pathway Links Completion of Cytokinesis to  
1149 Spindle Midzone Function to Prevent Chromosome Breakage. *Cell* **125**, 85–  
1150 98.
- 1151 **Oshima, K. and Fehon, R. G.** (2011). Analysis of protein dynamics within the  
1152 septate junction reveals a highly stable core protein complex that does not  
1153 include the basolateral polarity protein Discs large. *Journal of Cell Science*  
1154 **124**, 2861–2871.
- 1155 **Pannen, H., Rapp, T. and Klein, T.** (2020). The ESCRT machinery regulates  
1156 retromer-dependent transcytosis of septate junction components in  
1157 Drosophila. *Elife* **9**.
- 1158 **Peterman, E., Gibieža, P., Schafer, J., Skeberdis, V. A., Kaupinis, A., Valius, M.,**  
1159 **Heiligenstein, X., Hurbain, I., Raposo, G. and Prekeris, R.** (2019). The  
1160 post-abscission midbody is an intracellular signaling organelle that regulates  
1161 cell proliferation. *Nat Commun* **10**, 3181.

- 1162 **Pohl, C. and Jentsch, S.** (2009). Midbody ring disposal by autophagy is a post-  
1163 abscission event of cytokinesis. *Nat Cell Biol* **11**, 65–70.
- 1164 **R Core Team** (2022). R: A language and environment for statistical computing.p. R  
1165 Foundation for Statistical Computing, Vienna, Austria.
- 1166 **Raiborg, C. and Stenmark, H.** (2009). The ESCRT machinery in endosomal sorting  
1167 of ubiquitylated membrane proteins. *Nature* **458**, 445–452.
- 1168 **Rhyu, M. S., Jan, L. Y. and Jan, Y. N.** (1994). Asymmetric distribution of numb  
1169 protein during division of the sensory organ precursor cell confers distinct  
1170 fates to daughter cells. *Cell* **76**, 477–491.
- 1171 **Richard, M., Grawe, F. and Knust, E.** (2006). DPATJ plays a role in retinal  
1172 morphogenesis and protects against light-dependent degeneration of  
1173 photoreceptor cells in the *Drosophila* eye. *Dev Dyn* **235**, 895–907.
- 1174 **Scheffer, L. L., Sreetama, S. C., Sharma, N., Medikayala, S., Brown, K. J.,  
1175 Defour, A. and Jaiswal, J. K.** (2014). Mechanism of Ca<sup>2+</sup>-triggered ESCRT  
1176 assembly and regulation of cell membrane repair. *Nat Commun* **5**, 5646.
- 1177 **Shin, K., Fogg, V. C. and Margolis, B.** (2006). Tight junctions and cell polarity.  
1178 *Annu. Rev. Cell Dev. Biol.* **22**, 207–235.
- 1179 **Snow, P. M., Bieber, A. J. and Goodman, C. S.** (1989). Fasciclin III: a novel  
1180 homophilic adhesion molecule in *Drosophila*. *Cell* **59**, 313–323.
- 1181 **Steigemann, P., Wurzenberger, C., Schmitz, M. H. A., Held, M., Guizetti, J.,  
1182 Maar, S. and Gerlich, D. W.** (2009). Aurora B-Mediated Abscission  
1183 Checkpoint Protects against Tetraploidization. *Cell* **136**, 473–484.
- 1184 **Stork, T., Thomas, S., Rodrigues, F., Silies, M., Naffin, E., Wenderdel, S. and  
1185 Klämbt, C.** (2009). *Drosophila* Neurexin IV stabilizes neuron-glia interactions  
1186 at the CNS midline by binding to Wrapper. *Development* **136**, 1251–1261.
- 1187 **Sweeney, N. T., Brenman, J. E., Jan, Y. N. and Gao, F.-B.** (2006). The coiled-coil  
1188 protein shrub controls neuronal morphogenesis in *Drosophila*. *Curr Biol* **16**,  
1189 1006–1011.
- 1190 **Tempesta, C., Hijazi, A., Moussian, B. and Roch, F.** (2017). Boudin trafficking  
1191 reveals the dynamic internalisation of specific septate junction components in  
1192 *Drosophila*. *PLoS ONE* **12**, e0185897.
- 1193 **Tepass, U., Tanentzapf, G., Ward, R. and Fehon, R.** (2001). Epithelial cell polarity  
1194 and cell junctions in *Drosophila*. *Annu. Rev. Genet.* **35**, 747–784.
- 1195 **Tiklová, K., Senti, K.-A., Wang, S., Gräslund, A. and Samakovlis, C.** (2010).  
1196 Epithelial septate junction assembly relies on melanotransferrin iron binding  
1197 and endocytosis in *Drosophila*. *Nat Cell Biol* **12**, 1071–1077.
- 1198 **Tsukita, S., Furuse, M. and Itoh, M.** (2001). Multifunctional strands in tight  
1199 junctions. *Nat. Rev. Mol. Cell Biol.* **2**, 285–293.

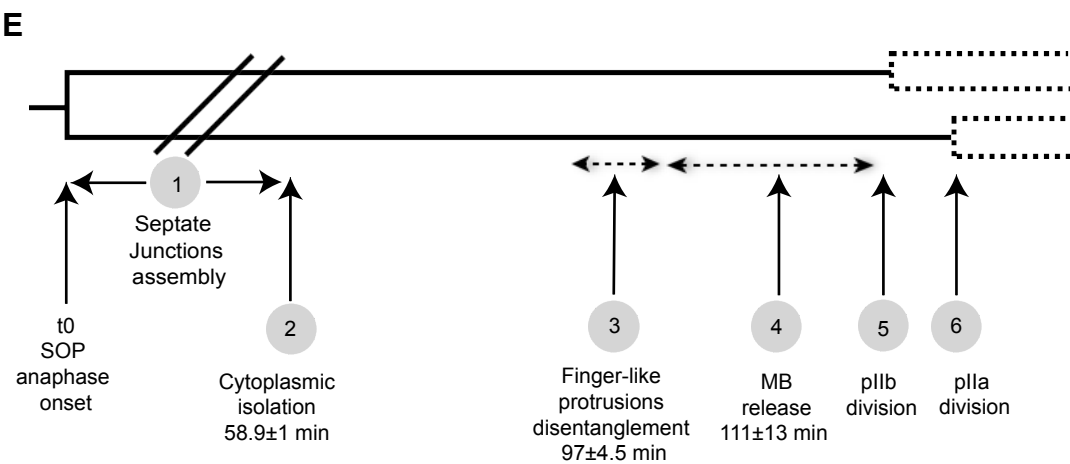
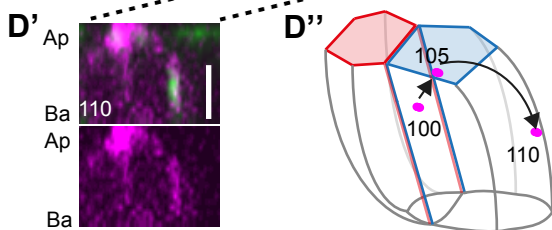
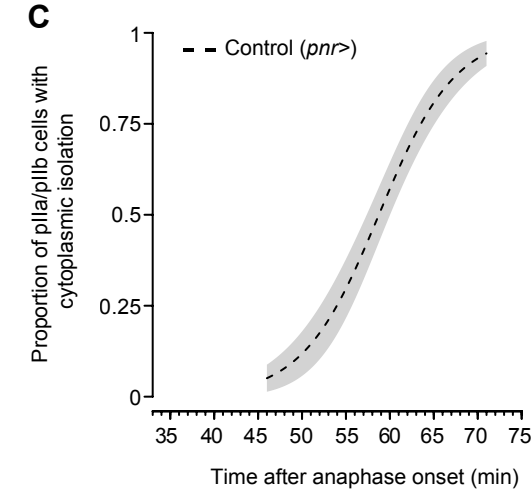
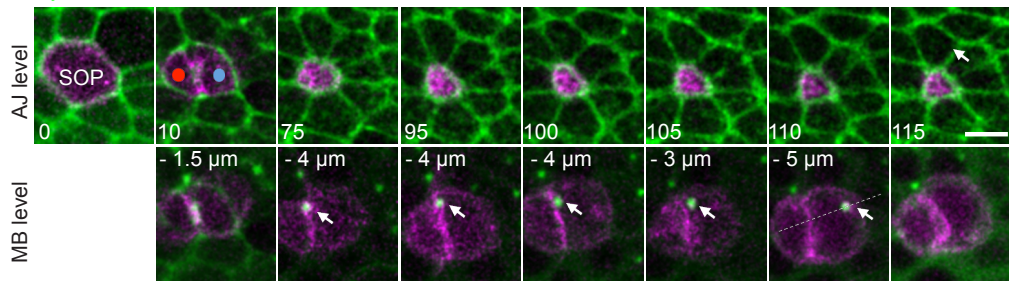
- 1200 **Vaccari, T., Rusten, T. E., Menut, L., Nezis, I. P., Brech, A., Stenmark, H. and**  
1201 **Bilder, D.** (2009). Comparative analysis of ESCRT-I, ESCRT-II and ESCRT-  
1202 III function in *Drosophila* by efficient isolation of ESCRT mutants. *J Cell Sci*  
1203 **122**, 2413–2423.
- 1204 **Vietri, M., Radulovic, M. and Stenmark, H.** (2020). The many functions of  
1205 ESCRTs. *Nat Rev Mol Cell Biol* **21**, 25–42.
- 1206 **Wang, Z., Bosveld, F. and Bellaïche, Y.** (2018). Tricellular junction proteins  
1207 promote disentanglement of daughter and neighbour cells during epithelial  
1208 cytokinesis. *J. Cell. Sci.* **131**,.
- 1209 **Ward, R. E., Lamb, R. S. and Fehon, R. G.** (1998). A conserved functional domain  
1210 of *Drosophila* coracle is required for localization at the septate junction and  
1211 has membrane-organizing activity. *J Cell Biol* **140**, 1463–1473.
- 1212 **Wu, V. M., Schulte, J., Hirschi, A., Tepass, U. and Beitel, G. J.** (2004). Sinuous is  
1213 a *Drosophila* claudin required for septate junction organization and epithelial  
1214 tube size control. *J Cell Biol* **164**, 313–323.
- 1215
- 1216
- 1217
- 1218

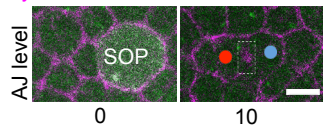
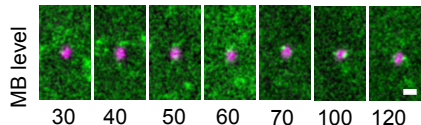


**A** MyoIIIRFP nlsRFP ATP $\alpha$ GFP H2BIR**B** MyoIIIRFP nlsRFP ATP $\alpha$ GFP H2BIR**C** MyoIIIRFP ATP $\alpha$ GFP GAP43IR**D** ATP $\alpha$ ::GFP recovery



**D** **MyoII**GFP **GAP43IR**



**A** MyoIIIRFP ShrbGFP GAP43IR**A'****A''**

pllb

pll a

First pool

**A'''**

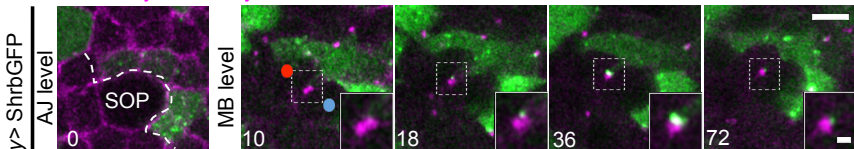
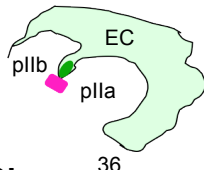
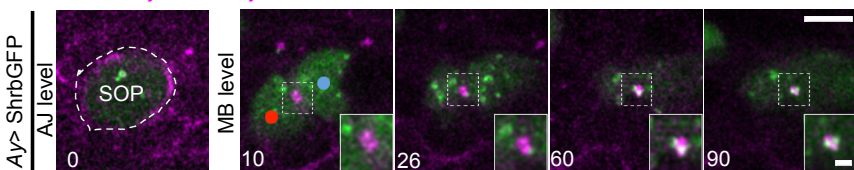
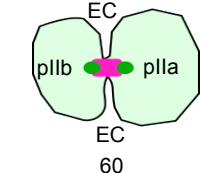
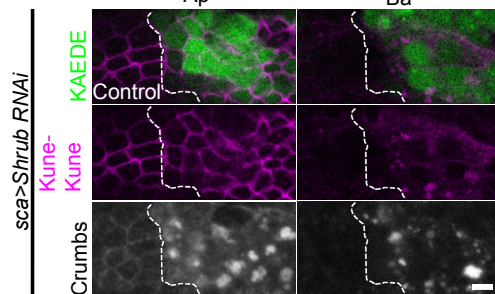
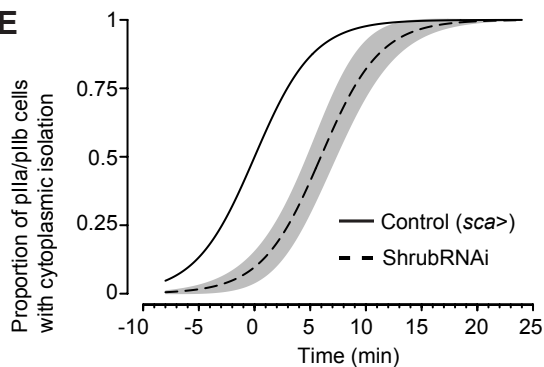
pll b

pll a

Second pool

Shrub

Midbody

**B** ShrbGFP MyoIIImcherry**B'****C** ShrbGFP MyoIIImcherry**C'****D****E**

**A**